Check for updates

JAMES | Journal of Advances in Modeling Earth Systems

RESEARCH ARTICLE
10.1029/2021MS002654

Key Points:

- A 3D sub-grid terrain radiative effect (STRE) scheme is developed
- The 3D STRE scheme can show more realistic description of the land surface solar radiation
- The CoLM coupled with the 3D STRE scheme significantly improved the simulation of soil thermal and moist features over complex terrain areas

Correspondence to:

A. Huang,
anhuang@nju.edu.cn

Citation:

Zhang, X., Huang, A., Dai, Y., Li, W., Gu, C., Yuan, H., et al. (2022). Influences of 3D sub-grid terrain radiative effect on the performance of CoLM over Heihe River Basin, Tibetan Plateau. *Journal of Advances in Modeling Earth Systems*, *14*, e2021MS002654. https://doi.org/10.1029/2021MS002654

Received 7 JUN 2021
Accepted 23 DEC 2021

Author Contributions:

Conceptualization: Anning Huang, Yongjiu Dai
Data curation: Xindan Zhang
Formal analysis: Xindan Zhang, Chunlei Gu, Shuxin Cai
Investigation: Xindan Zhang, Weiping Li
Methodology: Xindan Zhang, Anning Huang
Software: Xindan Zhang, Anning Huang, Chunlei Gu
Supervision: Anning Huang, Yongjiu Dai
Validation: Xindan Zhang
Visualization: Xindan Zhang
Writing – original draft: Xindan Zhang
Writing – review & editing: Anning Huang, Yongjiu Dai, Weiping Li, Hua Yuan, Nan Wei, Yanlin Zhang, Bo Qiu

© 2022 The Authors. Journal of Advances in Modeling Earth Systems published by Wiley Periodicals LLC on behalf of American Geophysical Union. This is an open access article under the terms of the Creative Commons Attribution-NonCommercial License, which permits use, distribution and reproduction in any medium, provided the original work is properly cited and is not used for commercial purposes.

Influences of 3D Sub-Grid Terrain Radiative Effect on the Performance of CoLM Over Heihe River Basin, Tibetan Plateau

Xindan Zhang[1], Anning Huang[1], Yongjiu Dai[2], Weiping Li[1,3], Chunlei Gu[1], Hua Yuan[2], Nan Wei[2], Yanlin Zhang[4], Bo Qiu[1], and Shuxin Cai[1]

[1]CMA-NJU Joint Laboratory for Climate Prediction Studies, State Key Laboratory of Severe Weather and Joint Center for Atmospheric Radar Research of CMA/NJU, School of Atmospheric Sciences, Nanjing University, Nanjing, China, [2]Guangdong Province Key Laboratory for Climate Change and Natural Disaster Studies, School of Atmospheric Sciences, Sun Yat-sen University, Guangzhou, China, [3]Laboratory for Climate Studies, National Climate Center, China Meteorological Administration (CMA), Beijing, China, [4]National-Local Joint Engineering Laboratory of Geo-Spatial Information Technology, Hunan University of Science and Technology, Xiangtan, China

Abstract Surface solar radiation (SSR), as a primary component of heat budget between land and atmosphere, controls both water and energy exchanges. However, the sub-grid terrain radiative effect (STRE) which exerts critical influences on SSR simulation is usually extremely simplified or even ignored in most current land surface models (LSMs) due to the heavy computational burden. In this study, we developed a physically realistic and computationally efficient three dimensional (3D) STRE scheme and implemented it into the Common Land Model (CoLM) to indicate its quantitative influences on surface energy budget, land surface temperature (LST), soil temperature, and moisture simulations over the Heihe River Basin, Tibetan Plateau. Results show that the CoLM coupled with 3D-STRE scheme shows more realistic description of SSR and improves the simulation of soil thermal and moist features at both single-point and regional scales. Compared to the results without 3D-STRE, the inclusion of 3D-STRE scheme efficiently diminishes the overestimation of SSR, which leads to the root mean square error (RMSE) of LST simulation reduced by 17.1% due to significant improvements in valley areas. Adopting 3D-STRE scheme also improves the pattern and amplitude of temporal variability of simulated soil temperature (moisture) at 37 sites with the mean Taylor score increased by 3.6–3.7% (14.0–14.3%). These results emphasize the importance of considering the 3D-STRE scheme in LSMs and are significantly helpful to deepen our understanding of surface heat exchanges and improve the representations of land surface processes over complex terrain.

Plain Language Summary Topography exerts remarkable influences on the land surface solar radiation (SSR) over complex terrain, which controls both water and energy exchanges between land and atmosphere. However, the parameterization of sub-grid topographical effects on SSR are usually extremely simplified or even ignored in most current numerical models due to the heavy computational burden. In this study, we developed a parameterization with much more real physical processes, simple parameters and high computational efficiency to consider the impact of sub-grid topography on SSR, it tends to show widely potential application in land process and climate modeling. Taking the Heihe River Basin in China as an example, we found that the land surface model coupled with this scheme shows more realistic description of SSR and significantly improves the simulations of soil thermal and moist features. These results highlight the necessity of considering the sub-grid topographical effects on SSR simulation in land surface modeling and are obviously helpful to advance our understanding of the surface heat exchanges and improve the representations of land surface processes over complex terrain areas.

1. Introduction

As a component of the surface heat budget, surface solar radiation (SSR) is the primary source of energy for the earth surface. It controls both water and energy exchanges between land surface and overlying atmosphere and is thus a major forcing for the land surface models, hydrological models, and ecological models (L. Chen et al., 2012; L. H. Gu et al., 2002; G. Huang et al., 2012; P. Huang et al., 2017; B. Tang et al., 2006; W. Tang et al., 2010; Vignola et al., 2007; T. Wang et al., 2012).

19422466, 2022, 1, Downloaded from https://agupubs.onlinelibrary.wiley.com/doi/10.1029/2021MS002654 by Anning Huang , Wiley Online Library on [22/03/2023]. See the Terms and Conditions (https://onlinelibrary.wiley.com/terms-and-conditions) on Wiley Online Library for rules of use; OA articles are governed by the applicable Creative Commons License

19422466, 2022, 1, Downloaded from https://agupubs.onlinelibrary.wiley.com/doi/10.1029/2021MS002654 by Anning Huang , Wiley Online Library on [22/03/2023]. See the Terms and Conditions (https://onlinelibrary.wiley.com/terms-and-conditions) on Wiley Online Library for rules of use; OA articles are governed by the applicable Creative Commons License

Regardless of cloud, aerosol and other atmospheric heterogeneities, topography is also one of the critical factors that jointly determines the spatial distribution of SSR. In general, the SSR striking on a tilted slope consists of direct and diffuse solar radiation and the reflected radiation from the surrounding terrain slopes (Dubayah & Loechel, 1997; Dubayah & Rich, 1995; Fu & Rich, 2002). On a flat terrain, the first two components dominate the SSR. However, in rough topography, the solar radiation reflected from surrounding slopes and obstructed by topographic features around becomes significant (Marsh et al., 2012).

Over the last three decades, the effects of topographical parameters such as slope, aspect, sky view factor and surrounding topographic shading have been systematically studied and a number of surface radiative transfer models (e.g., spherical harmonics discrete method, 3D Monte Carlo method and radiosity method) have been developed by using the topographic information contained in the reliable digital elevation model (DEM; Y. Chen & Liou, 2006; Y. Chen et al., 2006; Dozier & Frew, 1990; Evans, 1998; Fu, 1983; Helbig et al., 2009; Li et al., 1999; Ruiz-Arias et al., 2009, 2010, 2011; T. Wang et al., 2018; S. Wu et al., 2018). These models are more advantageous on small scales since they have taken fully subgrid-scale topographical effects into consideration to estimate the SSR in mountainous areas, which in turn exert significant improvements in the estimation of other surface parameters and energy fluxes. However, with the consideration of computational efficiency, most of the sub-grid scale terrain influences are usually extremely simplified or even ignored for large scale applications, such as meteorological models and hydrological models, which can bring about considerable systematic errors in land surface process simulation (Aguilar et al., 2010; Barry, 1992).

As the horizontal resolution of numerical models increase, terrain-induced effects of SSR at the sub-grid scale gain indispensable importance on simulations of surface energy balance and many climatic processes, including photosynthesis, snow melting, soil moistening and evapotranspiration. Muller and Scherer (2005) therefore introduced a parameterization based on a 1-km resolved elevation model into the Nonhydrostatic Mesoscale Model (NMM), demonstrating a general improvement of 0.5 K for RMSE and 1 K for mean error in the verification of 2-m air temperature, respectively. Liou et al. (2013) incorporated 3D mountainous effects on radiative transfer parameterization in the Weather Research and Forecasting (WRF) model to study the impacts on SSR and surface hydrology over the Sierra Nevada and Rocky Mountains. Results show that the WRF-simulated snow water equivalent and precipitation exhibit reasonable agreement with observations from Snowpack Telemetry sites in terms of the spatial patterns and daily and seasonal variability. A topographic solar radiation algorithm with the consideration of both slope self-shading and surrounding terrain shading has also been implemented into a geomorphologically based distributed hydrological model (Y. L. Zhang et al., 2018). An expectant model performance was achieved that the decrease of incident solar radiation estimation at the Babao River basin in China has led to the annual mean ground temperature reduced by 0.41°C and the evapotranspiration reduced by 16.1 mma^{-1}, respectively. Lee et al. (2019) investigated the radiation-topography interaction on the basis of Monte Carlo ray-tracing simulations and demonstrated its impact on the surface energy budget over Tibet Plateau (TP) in winter using the Community Climate System Model version 4 (CCSM4). Compared to observations and the ensemble of Coupled Model Intercomparison Project Phase 5 (CMIP5), the topographic effect reduces the essential biases of upward shortwave fluxes by increasing snow melt rate over the central and southern part of TP, consequently diminishing the simulated surface air temperature cold bias over TP by 13% in the CCSM4 model. C. Gu et al. (2020) has coupled a two dimensional sub-grid terrain radiative effect scheme into the Regional Climate Model Version 4.1 (RegCM4.1), correcting the overestimation of summer precipitation simulation over China due to the reduction of the net SSR over TP which attenuates the water vapor transport through the weakened East Asian summer monsoon resulted from the reduced TP thermal forcing and the weakened land-sea thermal contrast.

Although many meso-scale weather forecast models, land surface models and hydrological models have reconsidered the sub-grid topographic influence on SSR due to its incremental importance with the model horizontal resolution increasing in recent years, due to the heavy burden of computational efficiency and complexity in coupling process, the majority of current STRE schemes only include 2D topographical effects induced by terrain slope and aspect, while 3D shading and reflecting effects by the surrounding terrain are neglected, leading to noticeable overestimation of SSR in mountainous area during early morning and late afternoon (Arthur et al., 2018; C. Gu et al., 2020; Hauge & Hole, 2003; Shen & Hu, 2006; Y. Zhang et al., 2006). Besides, some investigators tended to find statistical relationships between sky view and shading factors and slope characteristics of real topographies in order to avoid complex integration calculations varying with solar elevation and azimuth (Essery & Marks, 2007;

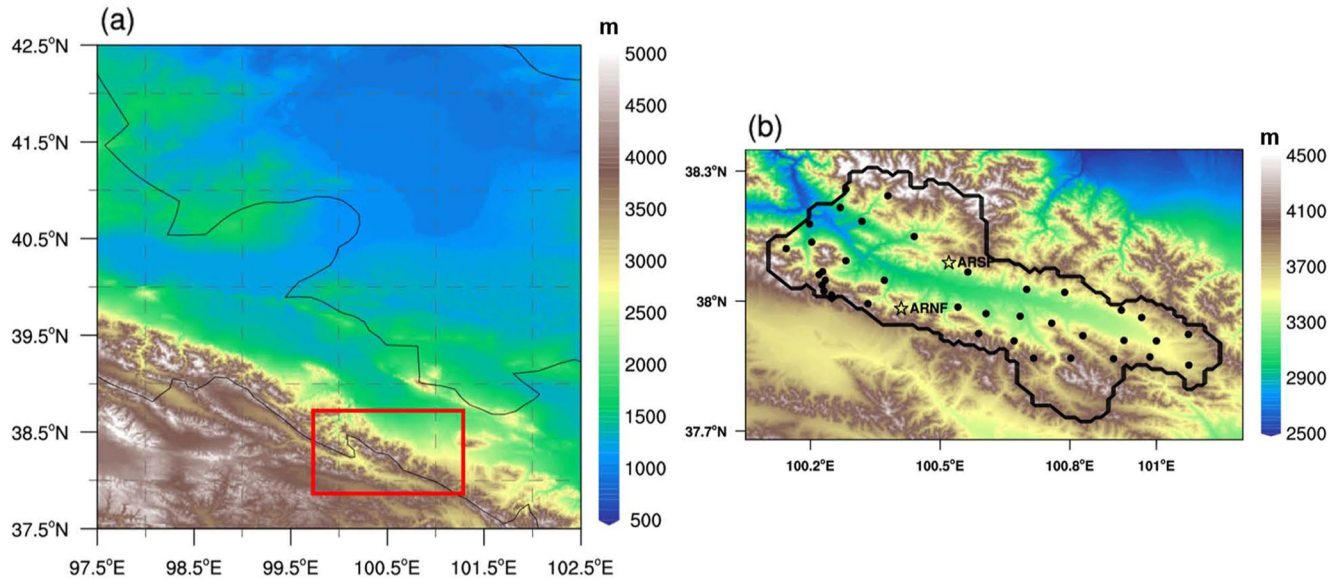

Figure 1. (a) Terrain elevation of the Heihe River basin with a resolution of 3 arc sec (~90 m). The red box indicates the upper branch of the Heihe River basin (b) with automatic weather stations (stars) and wireless network nodes (dots).

Helbig & Lowe, 2012; Helbig et al., 2009). However, such parameterizations were usually simulated under specific atmospheric radiative transfer schemes and validated based on actual radiations under influences of a limited ensemble of real landforms. It is questionable that whether these parameterization schemes trustworthy in their test area can show comparable performance and stronger portability in other mountainous areas.

For this reason, the objective of this study is to develop a common 3D-STRE scheme that is applicable for most numerical models and shares the virtues of relatively lower computational costs and more realistic description of SSR without explicitly resolving the SSR at sub-grid scale. Furthermore, we have also implemented this scheme into the Common Land Model (CoLM; Dai et al., 2003) to demonstrate the quantitative influences of sub-grid topographies on the surface heat budget and the thermal and hydrological processes in the Heihe River Basin over TP with complex terrain.

The paper is organized as follows: Section 2 briefly introduces an integrated 3D STRE approach and CoLM model, as well as data sets, numerical experiment design. The results of sensitivity experiment with and without 3D STRE scheme are presented in Section 3. Discussions are given in Section 4. Finally, Section 5 summarizes the main conclusions.

2. Model and Experimental Design

2.1. Study Area

This research focuses on the Heihe River Basin, which is the China's second largest inland river basin located in the northeastern margin of the TP. The Heihe River Basin spans Qinghai, Gansu, and Inner Mongolia provinces, with the Qilian Mountains in the southwest, the Hexi Corridor Plain in the middle, and is typical of most arid and semi-arid areas (Cheng et al., 2014), its main climate characters are dry, scarce and concentrated precipitation, strong winds, strong solar radiation, and large diurnal temperature range. The terrain of the entire basin varies drastically (Figure 1a), ranging approximately from 2,000 to 5,000 m over the upstream region and 800–1,700 m over the downstream region (S. Liu et al., 2018), causing great heterogeneity of the spatial distribution of SSR, which in turn requires that the influence of topography must be taken into account to help increase the accuracy of SSR as an important forcing for CoLM and further improve the model performance in simulating the soil thermal and hydrologic features. Additionally, the Heihe integrated observatory network conducted by the Watershed Allied Telemetry Experimental Research (WATER, Li et al., 2009) and the Heihe Watershed Allied Telemetry Experimental Research (HiWATER, Li et al., 2013) collects abundant long-term observational data and provides significant benefits for the validation and improvement of LSMs performance.

19422466, 2022, 1, Downloaded from https://agupubs.onlinelibrary.wiley.com/doi/10.1029/2021MS002654 by Anning Huang , Wiley Online Library on [22/03/2023]. See the Terms and Conditions (https://onlinelibrary.wiley.com/terms-and-conditions) on Wiley Online Library for rules of use; OA articles are governed by the applicable Creative Commons License

19422466, 2022, 1, Downloaded from https://agupubs.onlinelibrary.wiley.com/doi/10.1029/2021MS002654 by Anning Huang , Wiley Online Library on [22/03/2023]. See the Terms and Conditions (https://onlinelibrary.wiley.com/terms-and-conditions) on Wiley Online Library for rules of use; OA articles are governed by the applicable Creative Commons License

2.2. Model Description

The CoLM model (Dai et al., 2003) which has been developed from the initial version of the Community Land Model (CLM), combines the advantages of three well-known models: the National Center for Atmospheric Research (NCAR) land surface model (Bonan, 1996), the Biosphere-Atmosphere Transfer Scheme (BATS; Dickinson et al., 2010), and the 1994 version of the Institute of Atmospheric Physics LSM (IAP94; Dai & Zeng, 1997). The CoLM model includes a two-big-leaf model for photosynthesis, the pedotransfer functions for soil hydraulic and thermal parameters, the numerical solution of the Richards equation for soil water content and the groundwater. Various studies have shown that the CoLM can reasonably simulate the energy allocation patterns and land surface state in the high-altitude arid areas of northwestern China and TP (Luo et al., 2009; Song et al., 2008; Xin et al., 2006).

In current CoLM, the plane-parallel radiative transfer model adopts an empirical expression to separate downward solar irradiance (E) on a flat surface into direct fluxes $E_{dir,v}$, $E_{dir,n}$ and diffuse fluxes $E_{dif,v}$ and $E_{dif,n}$, where the subscript v and n indicate the visible band and the near-infrared band of solar fluxes, respectively. The simplified radiation parameterization scheme neglects significant physical process for radiative transfer induced by sub-grid topography, which will be introduced and implemented into the CoLM model in current study.

2.3. The 3D-SRTE Parameterization Scheme

2.3.1. Calculation of SSR at Single Point Over Mountainous Area

To introduce the topographic effects into the conventional radiative transfer scheme, the surface solar radiative fluxes at a incline plane can be recomposed by three components: direct ($E_{dir,t}$), diffuse ($E_{dif,t}$), and surrounding-reflected irradiances ($E_{ref,t}$), given the subgrid-scale orographic information including terrain slope, aspect, the sky view factor (SVF) and terrain shading factor (SF), where subscript t denotes the fluxes on terrain. Solar fluxes on a target subgrid point i at the mountain surface can be expressed as follows (Li & Li, 2007; Li et al., 2002):

$$E_{dir,t_i} = \begin{cases} \dfrac{E_{dir_i}}{\cos Z_i} \mathrm{SF}_i \ \cos\gamma_i, & \text{if } \cos\gamma_i > 0 \text{ and } \cos Z_i > 0 \\ 0, & \text{otherwise} \end{cases} \tag{1}$$

$$E_{dif,t_i} = \begin{cases} E_{dif_i}\left[\dfrac{E_{dir,t_i}}{E_{ac}} + \mathrm{VD}_i\left(1 - \dfrac{E_{dir_i}}{E_{ac}}\right)\right], & \text{if } \cos\gamma_i > 0 \text{ and } \cos Z_i > 0 \\ E_{dif_i}\left[\mathrm{VD}_i\left(1 - \dfrac{E_{dir_i}}{E_{ac}}\right)\right], & \text{otherwise} \end{cases} \tag{2}$$

$$E_{ref,t_i} = \frac{1}{2}(E_{dir_i} + E_{dif_i})\rho_i(1 - \cos\alpha_i) \tag{3}$$

where E_{dir_i} and E_{dif_i} are incident direct and diffusive solar radiative fluxes at plane, respectively. The solar constant $E_{ac} = 1{,}367\ \mathrm{Wm}^{-2}$ and ρ denotes the surface albedo. γ is the solar incident angle on a sloped grid i, which varies with the solar zenith angle (Z) and solar azimuth angle (ϕ), slope (α), and aspect (β) of the surface pixel (Figure 2a) and is calculated as:

$$\cos\gamma = \cos Z \ \cos\alpha + \sin\alpha \ \cos\beta \ \sin Z \ \cos\phi + \sin\alpha \ \sin\beta \ \sin Z \ \sin\phi \tag{4}$$

The solar azimuth angle ϕ defined as the angle between a line due north and the projection of solar light on the horizontal plane can be calculated as the following formula (Reda & Andreas, 2007):

$$\cos\phi = \frac{\sin\delta - \cos Z \ \sin\varphi}{\sin Z \ \cos\varphi} \tag{5}$$

where δ, φ are solar declination and latitude. While, the α and β can be expressed by the gradient of the elevation H (Y. Zhang et al., 2006):

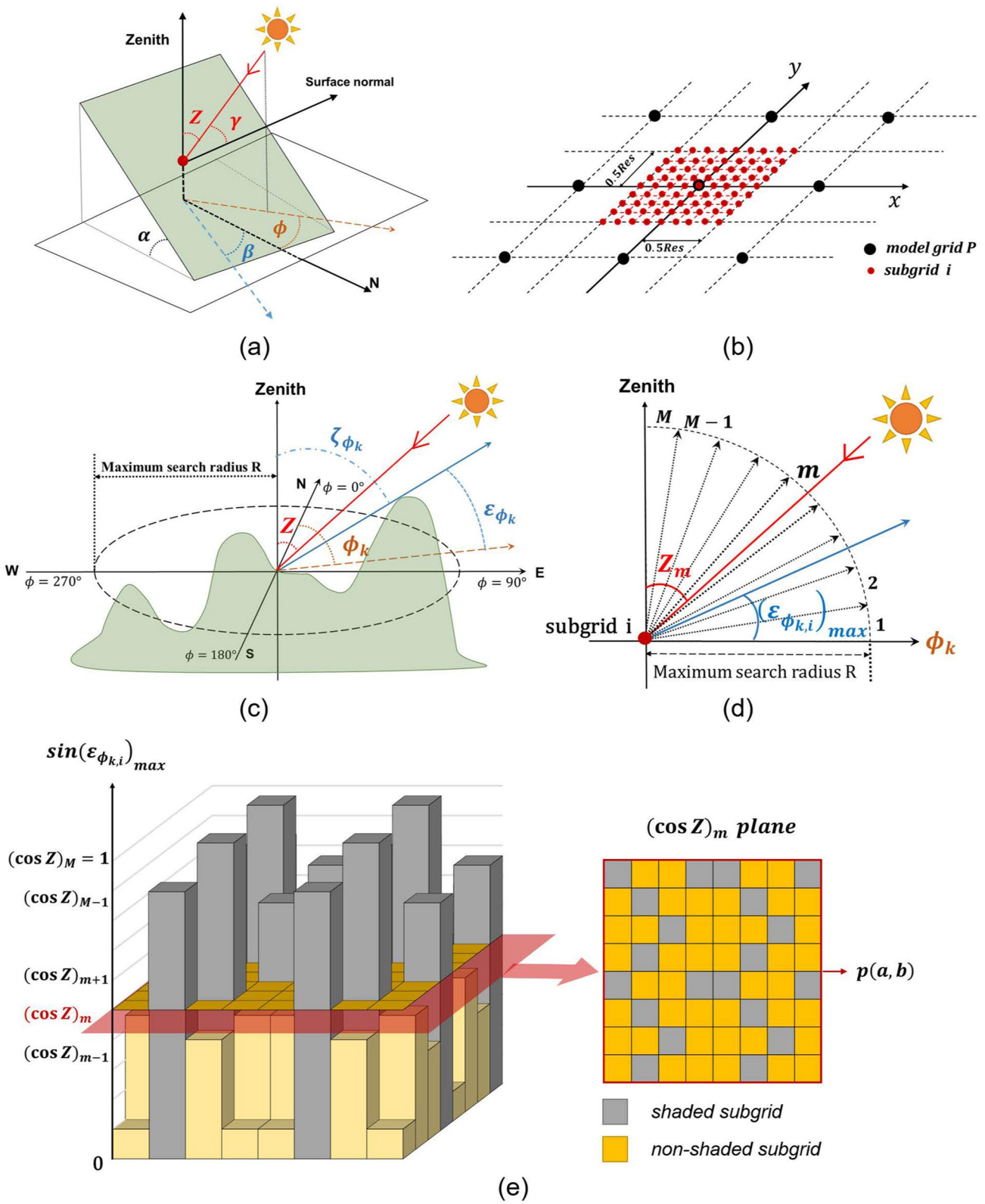

Figure 2. (a) Schematic representations for an incident solar beam on an inclined surface and (b) for subgrid cells in a model grid. (c) Schematic representations for explicitly calculating the sky view factor and (d) the shading factor in a sub grid. (e) Schematic representation for the parameterization of a shading factor in one model grid.

19422466, 2022, 1, Downloaded from https://agupubs.onlinelibrary.wiley.com/doi/10.1029/2021MS002654 by Anning Huang , Wiley Online Library on [22/03/2023]. See the Terms and Conditions (https://onlinelibrary.wiley.com/terms-and-conditions) on Wiley Online Library for rules of use; OA articles are governed by the applicable Creative Commons License

$$\alpha = \text{arctg}\sqrt{\left(\frac{\partial H}{\partial x}\right)^2 + \left(\frac{\partial H}{\partial y}\right)^2} \tag{6}$$

$$\beta = \begin{cases} \frac{3\pi}{2} - \text{arctg}\left(\frac{\frac{\partial H}{\partial y}}{\frac{\partial H}{\partial x}}\right), & \text{if } \frac{\partial H}{\partial x} > 0 \\ \frac{\pi}{2} - \text{arctg}\left(\frac{\frac{\partial H}{\partial y}}{\frac{\partial H}{\partial x}}\right), & \text{if } \frac{\partial H}{\partial x} < 0 \\ 0, & \text{if } \frac{\partial H}{\partial x} = 0 \ \ \frac{\partial H}{\partial y} < 0 \\ \pi, & \text{if } \frac{\partial H}{\partial x} = 0 \ \ \frac{\partial H}{\partial y} > 0 \\ \text{undefined}, & \text{if } \frac{\partial H}{\partial x} = 0 \ \ \frac{\partial H}{\partial y} = 0 \end{cases} \tag{7}$$

The diffusive parameter VD is equal to 1/2 SVF$(1 + \cos\alpha)$, in which the sky view factor (SVF) is parameterized as the ratio of the visible sky for a target slope to the area for an unobstructed semi-sphere on the horizontal surface, which ranges from 0 to 1 dependent on the obstruction from the adjacent terrains. SVF close to 0 represents the target point lies in the low land of a deep valley. On the opposite, SVF = 1 when the target point is in an exposed feature like a plane or a peak. The SVF algorithm adopted in this study was proposed by Dozier and Frew (1990):

$$\text{SVF} = \frac{1}{N}\sum_{k=1}^{N}[\cos\alpha \ \ \sin^2\zeta_{\phi_k} + \sin\alpha \ \ \cos(\phi_k - \beta)(\zeta_{\phi_k} - \sin\zeta_{\phi_k} \ \ \cos\zeta_{\phi_k})] \tag{8}$$

where N is the number of horizontal searching directions, ζ_{ϕ_k} (Figure 2c) denotes the angle between the connection line (from the adjacent point with the maximum shading effect to the target point) and the vertical line at the target point in the kth discretized azimuth angle ϕ_k. The SF is the obstruction coefficient, which indicates whether the objective point is shaded by the intervening topography in the solar azimuth angle ϕ. As shown in Figure 2c, ε_{ϕ_k} denotes the angle between the connection line (from the adjacent point with the maximum shading effect to the target point) and the horizontal line at the target point in the kth discretized azimuth angle ϕ_k. The SF is equal to 1 when ε_{ϕ_k} is smaller than or equal to the solar elevation angle ($\sin\varepsilon_{\phi_k} \le \cos Z$), representing the direct radiation is entirely received by the objective point. Otherwise, no direct radiation reaches when SF is equal to 0 ($\sin\varepsilon_{\phi_k} > \cos Z$). Unlike the other STRE parameters can be completely preprocessed before running the model, the SF is a time-variant variable that jointly determined by the solar azimuth angle ϕ and the solar zenith angle Z, and needs to be updated at every model time step. Therefore, as the horizontal resolutions of numerical models increase, detailed processing for the sub-grid surface solar radiative flux calculation and sub-grid STRE parameters will obviously limit the computational efficiency, and should not be explicitly computed during model time integration.

2.3.2. The 3D STRE Parameterization Scheme and Its Application in CoLM

To balance the model performance and computational efficiency with the model horizontal resolution increasing, the 3D STRE parameterization scheme should be implemented in the CoLM to compute the SSR with the calibration of the preprocessed parameters of 3D STRE scheme at the model grid resolution which contain abundant sub-grid topography characteristics.

Based on 2D-STRE scheme proposed by C. Gu et al. (2020), the solar incident angle for the model grid p can be written as:

$$(\cos\gamma)_p = <\cos\gamma_i>_{i\to p} \tag{9}$$

19422466, 2022, 1, Downloaded from https://agupubs.onlinelibrary.wiley.com/doi/10.1029/2021MS002654 by Anning Huang , Wiley Online Library on [22/03/2023]. See the Terms and Conditions (https://onlinelibrary.wiley.com/terms-and-conditions) on Wiley Online Library for rules of use; OA articles are governed by the applicable Creative Commons License

19422466, 2022, 1, Downloaded from https://agupubs.onlinelibrary.wiley.com/doi/10.1029/2021MS002654 by Anning Huang , Wiley Online Library on [22/03/2023]. See the Terms and Conditions (https://onlinelibrary.wiley.com/terms-and-conditions) on Wiley Online Library for rules of use; OA articles are governed by the applicable Creative Commons License

where the operator $<>_{i\to p}$ represents the mean values of a given variable at the sub-grids within the model grid p (Figure 2b). With the assumption that all sub-grid solar zenith angles and solar azimuth angles are uniformly distributed in a model grid, namely $Z_i \doteq Z_p$ and $\phi_i \doteq \phi_p$, Equation 9 can be rewritten according to Equation 4 as

$$(\cos\gamma)_p = u_p\ \cos Z_p + v_p\ \sin Z_p\ \cos\phi_p + w_p\ \sin Z_p\ \sin\phi_p \tag{10}$$

where

$$\begin{cases} u_p = <\cos\alpha_i>_{i\to p} \\ v_p = <\sin\alpha_i\ \cos\beta_i>_{i\to p} \\ w_p = <\sin\alpha_i\ \sin\beta_i>_{i\to p} \end{cases} \tag{11}$$

For the 3D-STRE scheme, the calibrators $(\cos\alpha)_p$ and $(\mathrm{VD})_p$ independent on time can be simply obtained by:

$$(\cos\alpha)_p = <\cos\alpha_i>_{i\to p} = u_p \tag{12}$$

$$\mathrm{VD}_p = <\mathrm{VD}_i>_{i\to p} \tag{13}$$

while the calculation for the time-dependent SF_p should be decomposed into two steps. First, we should prepare a time-invariant four-dimensional array A(*Inum*, *Jnum*, *N*, *M*) that comprises of terrain shading conditions for all sub-grids in distributed solar elevation angles along different solar azimuth angles, where *Inum* and *Jnum* denote the numbers of model grids in the longitudinal and latitudinal directions, respectively. Practically speaking, we divided the cosine of solar zenith angle into *M* levels (Figure 2d) and separated the solar azimuth angles into *N* directions. Thus, given a solar azimuth angle in the *k*th direction, we count the number of non-shaded sub-grids within a model grid $p(a, b)$ (a and b represent the number of the model grid p in the longitudinal and latitudinal directions, respectively) through comparing the sine value of the maximum terrain shading elevation angle $\sin(\varepsilon_{\phi_{k,i}})_{\max}$ of each sub-grid i with the mth level of the cosine of solar zenith angle $(\cos Z)_m$ (when $\sin(\varepsilon_{\phi_{k,i}})_{\max} \le \cos Z_m$, the sub-grid i will be taken into account, as shown in Figure 2e) and denote it as n_m. Supposing that one model grid contains n sub-grids, n_m/n represents the shading condition of all sub-grids in a model grid $p(a, b)$ ranging from 0 to 1 (zero for completely shadowed). It is the exact same analogy that n_1/n, n_2/n, …, n_m/n include shading conditions of the model grid $p(a, b)$ from all levels of the cosine of solar zenith angle in the kth searching direction, and then would be saved into the four-dimensional array A(a , b, k, m). After searching from all directions for every model grid, a time-invariant matrix A(*Inum*, *Jnum*, *N*, *M*) is obtained in advance before the model integration. During the model time integration, the SF_p at model grid $p(a, b)$ is finally gained by the nearest order of k and m for the corresponding ϕ_p and Z_p and equals to A(a, b, k, m).

Overall, we can couple the 3D STRE scheme into the CoLM by three steps (Figure 3). First, before running the model, we should calculate the calibration factors u_p, v_p, w_p, VD_p and A(*Inum*, *Jnum*, *N*, *M*) corresponding to a given model horizontal resolution in advance according to Equations 11–13. Second, we use ϕ_p and Z_p computed by CoLM already during the model time integration to calculate the rest calibrators $(cos\ \gamma)_p$ and SF_p based on Equation 10. Finally, we compute the three components of SSR at each model grid by substituting all these calibration factors, the equations for the 3D STRE parameterization scheme are as follows:

$$E_{dir,t_p} = \begin{cases} \dfrac{E_{dir_p}}{\cos Z_p}\mathrm{SF}_p(\cos\gamma)_p, & \mathrm{if}(\cos\gamma)_p > 0\ \text{ and }\ \cos Z_p > 0 \\ 0, & \text{otherwise} \end{cases} \tag{14}$$

$$E_{dif,t_p} = \begin{cases} E_{dif_p}\left[\dfrac{E_{dir,t_p}}{E_{ac}} + \mathrm{VD}_p\left(1 - \dfrac{E_{dir_p}}{E_{ac}}\right)\right], & \mathrm{if}(\cos\gamma)_p > 0\ \text{ and }\ \cos Z_p > 0 \\ E_{dif_p}\left[\mathrm{VD}_p\left(1 - \dfrac{E_{dir_p}}{E_{ac}}\right)\right], & \text{otherwise} \end{cases} \tag{15}$$

$$E_{ref,t_p} = \frac{1}{2}(E_{dir_p} + E_{dif_p})\rho_p(1 - u_p) \tag{16}$$

19422466, 2022, 1, Downloaded from https://agupubs.onlinelibrary.wiley.com/doi/10.1029/2021MS002654 by Anning Huang , Wiley Online Library on [22/03/2023]. See the Terms and Conditions (https://onlinelibrary.wiley.com/terms-and-conditions) on Wiley Online Library for rules of use; OA articles are governed by the applicable Creative Commons License

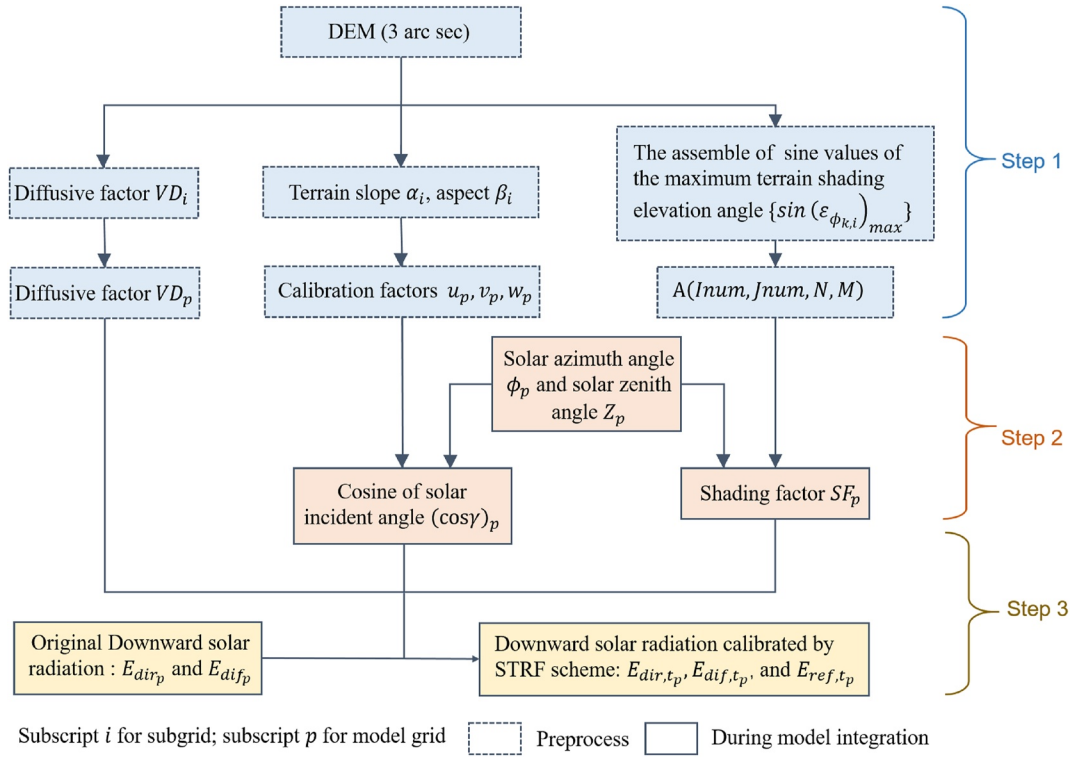

Figure 3. The summary flowchart for coupling the 3D STRE scheme into the CoLM.

The STRE parameters including terrain slope, aspect, SVF and SF were calculated based on the Shuttle Radar Topography Mission (SRTM) global data set (Jarvis et al., 2008, available at http://srtm.csi.cgiar.org) with a resolution of 3 arc sec (~90 m), which ensures that the sub-grid terrain in the CoLM model can be well represented. Accuracy of the SVF and SF calculations is largely dependent on the maximum research radius (R), the number (N) of distributed azimuth angles and the number (M) of discretized solar elevation angles. In this study, we set $N = 240$, $M = 100$ and $R = 9$ km (100 sub-grids with the resolution of 90 m) in consideration of the balance between the precision with the minimization of computational demand. The STRE parameters u, v, w and VD at sub-grid resolution and model resolution are respectively illustrated in Figure 4. The parameter u (Figures 4a and 4e) over complex terrain is smaller than that over the flat region due to its dependence on the terrain slope. Both v and w are highly subject to the terrain aspect that the positive value of v means the slope is facing the north, while the positive value of w represents for an east-faced slope. As shown in Figures 4d and 4h, the sub-grid topographic effects induced by the VD are reasonably reproduced at the model resolution. Figure 5 displays the diurnal variations of the SF on 1 July 2014 over the model domain, the SF varies drastically in correspondence with the changes in the solar zenith and azimuth angles. At 8:00 and 18:00 of the local time (Figures 5a and 5c), strong shadow effects are found in the northwest of the Heihe River Basin and along the Qilian Mountains, while the spatial variations of the SF are noticeably smaller during the noon time (Figure 5b).

2.4. Data and Experimental Design

2.4.1. Data

The hourly atmospheric forcing data (Pan, 2020; Pan & Ma, 2019; Pan et al., 2012, 2015; available at http://poles.tpdc.ac.cn) used to conduct off-line simulations of CoLM are output of WRF model especially over the Heihe River Basin with a horizontal resolution of 0.05° × 0.05° from 1 January 2013 to 31 December 2015, including 2 m air temperature, 2 m specific humidity, precipitation, atmospheric pressure at surface, 10 m wind in eastward and northward directions, surface downward solar radiation and atmospheric longwave radiation, which have been validated by the daily meteorological observation data from 15 stations of China Meteorological Administration (CMA) and hourly meteorological observation data from several sites of Heihe Watershed Allied

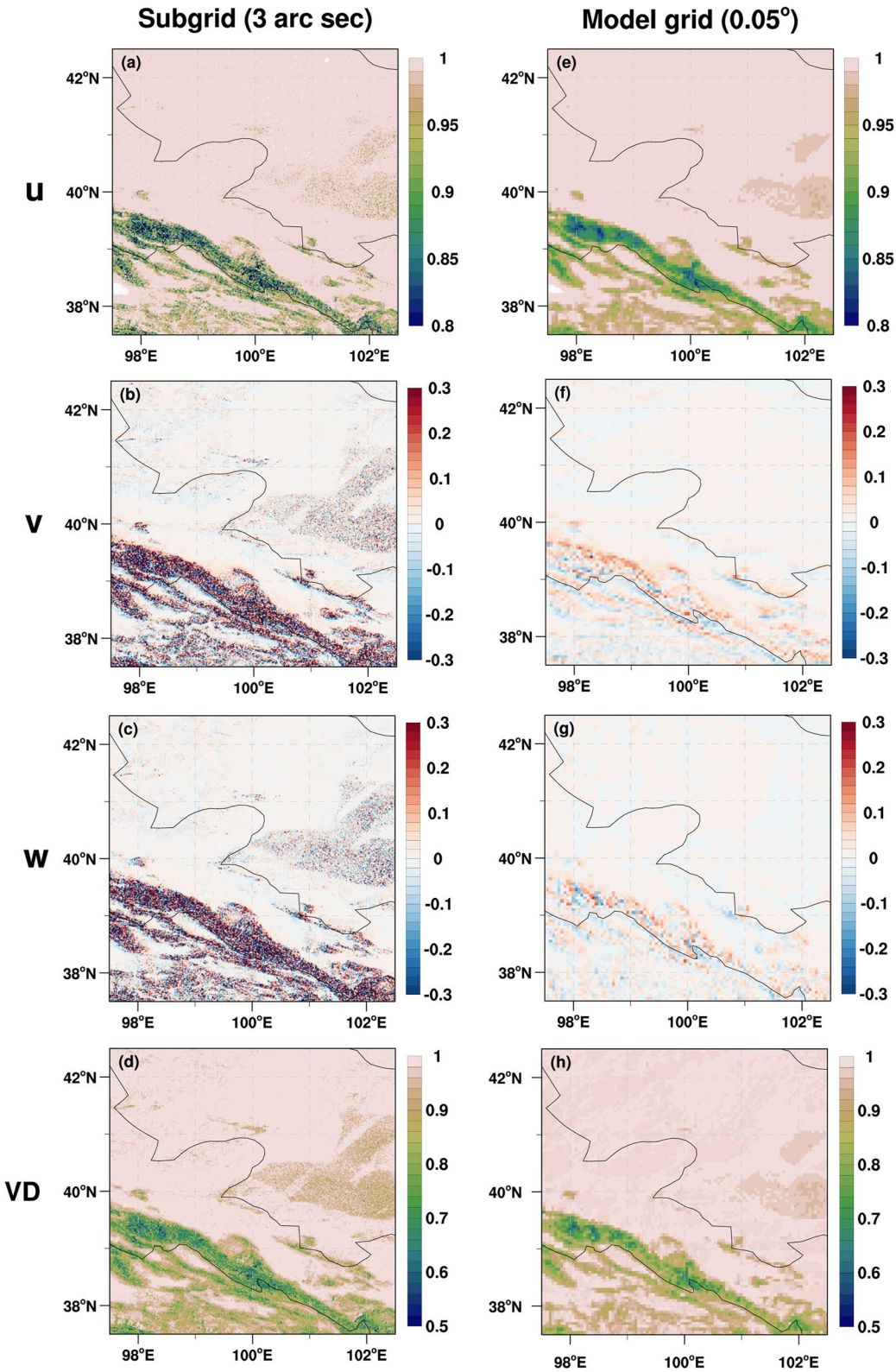

Figure 4. The spatial distributions of time-invariant STRE factors *u*, *v*, *w* and VD in the subgrid resolution (3 arc sec, the left column) and in the model resolution (0.05°, the right column) respectively.

19422466, 2022, 1, Downloaded from https://agupubs.onlinelibrary.wiley.com/doi/10.1029/2021MS002654 by Anning Huang , Wiley Online Library on [22/03/2023]. See the Terms and Conditions (https://onlinelibrary.wiley.com/terms-and-conditions) on Wiley Online Library for rules of use; OA articles are governed by the applicable Creative Commons License

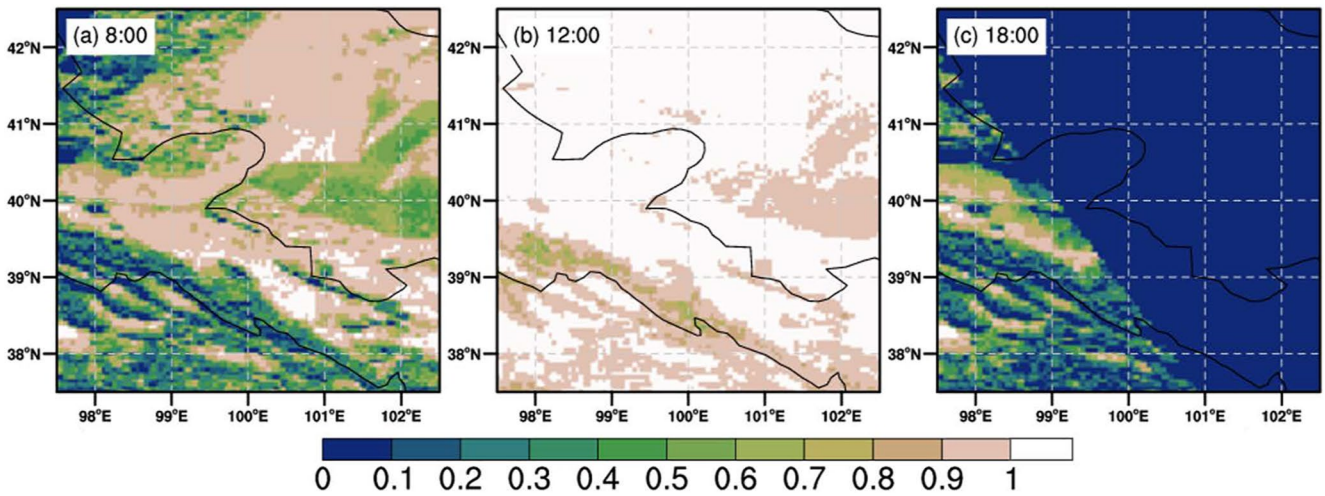

Figure 5. Spatial distribution of the SF (a) in the morning 8:00 BJT, (b) at noon 12:00 BJT and dusk (c) 18:00 BJT on 1 July 2014.

Telemetry Experimental Research (HIWATER). The validation results show that 2 m air temperature and surface pressure are dependable that their average errors are very small and the temporal correlation are above 0.96. The correlation coefficient between surface downward solar radiation and observation data from the HIWATER are over 0.8.

Additionally, the data sets used for model validation are listed as follows: (a) The daily mean Global Land Surface Satellite (GLASS) downward surface solar radiation product with a horizontal resolution of 5 km (X. Zhang et al., 2014, 2016, available at http://www.geodata.cn); (b) the land surface temperature (LST) product for China at monthly resolution on a $0.05° \times 0.05°$ spatial grid, reconstructed by a combination of Terra and Aqua MODIS daily data and meteorological station data (Mao, 2020; Zhao et al., 2020, available at http://poles.tpdc.ac.cn), hereafter OBS; (c)The daily evapotranspiration data at a spatial resolution of 100m derived from the revised Surface Energy Balance System (SEBS) model driven by the MODIS surface parameters data combined with the Landsat Enhanced Thematic Mapper Plus (ETM+) data (S. Liu et al., 2018; Ma & Liu, 2020; Ma et al., 2018), which shows good agreement with the ground measurements from 18 eddy covariance sites in the Heihe River Basin; (d) The observation data including downward solar radiation, surface temperature, soil temperature and moisture were collected at two automatic weather stations ARNF and ARSF from HIWATER (stars in Figure 1b) with the temporal resolution of 10 min (Che et al., 2019; S. M. Liu et al., 2016a, 2016b, 2018); (e) Besides, an ecological and hydrological wireless sensor network (WSN) has been installed at the upper reach of the Heihe River Basin to collect the soil temperature and soil moisture information at the depth of 4 and 20 cm with 5-min intervals (Che et al., 2019; Jin et al., 2014, 2015, available at http://poles.tpdc.ac.cn). We have then aggregated these data from 37 nodes of the WSN (dots in Figure 1b) into daily series with quality control during 1 January 2014 to 31 December 2014.

2.4.2. Experimental Design

To indicate the impact of the 3D STRE scheme on the simulation of surface energy budget, soil temperature and moisture, we set up two groups of experiments in current study. The first group of experiments namely STRE_SExp and Default_SExp in which the single point simulation is carried out using the CoLM with and without the 3D STRE scheme, respectively. The single point simulations at ARNF and ARSF stations were driven by the hourly atmospheric forcing data of WRF from 1 January 2014 to 31 December 2014 interpolated onto the two stations, in which the precipitation data were replaced by the actual data collected at the two stations, and the in-situ observed soil temperature and moisture data on 1 January 2014 were used as the initial soil condition profile. The second group of experiments are carried out in regional simulations with the 3D SRTE scheme turned on (called STRE_RExp) and off (called Default_RExp) in the CoLM model. In regional experiments, the model time step is set to 60 min and the model horizontal resolution is set to 0.05° (~5 km) in latitude and 0.05° in longitude. Offline regional simulations were performed for 12 years cyclically driven by the atmospheric forcing data from

19422466, 2022, 1, Downloaded from https://agupubs.onlinelibrary.wiley.com/doi/10.1029/2021MS002654 by Anning Huang , Wiley Online Library on [22/03/2023]. See the Terms and Conditions (https://onlinelibrary.wiley.com/terms-and-conditions) on Wiley Online Library for rules of use; OA articles are governed by the applicable Creative Commons License

19422466, 2022, 1, Downloaded from https://agupubs.onlinelibrary.wiley.com/doi/10.1029/2021MS002654 by Anning Huang , Wiley Online Library on [22/03/2023]. See the Terms and Conditions (https://onlinelibrary.wiley.com/terms-and-conditions) on Wiley Online Library for rules of use; OA articles are governed by the applicable Creative Commons License

1 January 2013 to 31 December 2015 and the last three years were extracted for subsequent analysis, so as to fully transfer thermal signals introduced by the 3D STRE effects into deep soil layers.

2.5. Methodology

Four statistical metrics were adopted for the quantitative analysis in this study to evaluate the performance of the CoLM simulations: the mean bias error (MBE), the root mean squared error (RMSE), the relative error (RE) and the correlation coefficient (R). These statistical metrics are expressed as:

$$\mathrm{MBE} = \frac{1}{n}\sum_{i=1}^{n}(s_i - o_i) \tag{17}$$

$$\mathrm{RMSE} = \sqrt{\frac{1}{n}\sum_{i=1}^{n}(s_i - o_i)^2} \tag{18}$$

$$\mathrm{RE} = \frac{s - o}{o} \times 100\% \tag{19}$$

$$R = \frac{\sum_{i=1}^{n}(s_i - \bar{s})(o_i - \bar{o})}{\sqrt{\sum_{i=1}^{n}(s_i - \bar{s})^2 \sum_{i=1}^{n}(o_i - \bar{o})^2}} \tag{20}$$

where s_i and o_i represent the simulation and observation at the ith point, respectively. The MBE, RE, and RMSE are used to indicate the mode errors. R gives the temporal or spatial correlation between the simulation and observation.

In addition, the Taylor score (TS; Taylor, 2001) expressed as follows was adopted to validate the model simulation in the amplitude and pattern of variability simultaneously.

$$\mathrm{TS} = \frac{4(1+R)}{\left(\sigma + \frac{1}{\sigma}\right)^2 (1 + R_0)} \tag{21}$$

$$\sigma = \frac{\sqrt{\frac{1}{n}\sum_{i=1}^{n}(s_i - \bar{s})^2}}{\sqrt{\frac{1}{n}\sum_{i=1}^{n}(o_i - \bar{o})^2}} \tag{22}$$

where R is given by Equation 20 and R_0 is the maximum correlation usually set to 1. The σ is the ratio between the standard deviations of simulations and observations. The TS ranges from 0 to 1 and higher Taylor score indicates better performance in simulating the amplitude and pattern of variability (A. Huang et al., 2016; Kan et al., 2015).

3. Results

3.1. Validation of the Single-Point Simulation

We first apply the CoLM coupled with the 3D STRE scheme to conduct single-point simulation at the two automatic weather stations named ARNF and ARSF which are remarkably shadowed by surrounding landform based on the developed terrain parameter datasets. Table 1 lists the geographical characters and the MBE, RMSE and R values of the hourly simulated SSR and LST against observation at the two stations. Compared to the Default_SExp, the STRE_SExp with the 3D STRE scheme significantly reduces the MBE of SSR (LST) by more than 15 W m^{-2} (0.4°C) at each site. Meanwhile, the RMSE values of the simulated SSR and LST in the STRE_SExp are also obviously reduced. Especially for the ARNF site, the RMSE values for the SSR and LST are reduced by ~10 W m^{-2} (improved by ~7%) and 2.75°C (improved by ~40%) respectively, with the temporal correlation coefficient of LST increased by 0.13 (~18%). The validations of the daily SSR and LST in Figure 6 further shows that the daily SSR and LST simulated by the STRE_SExp with the terrain effect are in good agreement with the observation at the ARNF site relative to the Default_SExp.

19422466, 2022, 1, Downloaded from https://agupubs.onlinelibrary.wiley.com/doi/10.1029/2021MS002654 by Anning Huang , Wiley Online Library on [22/03/2023]. See the Terms and Conditions (https://onlinelibrary.wiley.com/terms-and-conditions) on Wiley Online Library for rules of use; OA articles are governed by the applicable Creative Commons License

Table 1
Geographical Characters and Hourly MBE, RMSE and R Values of Simulated SSR and LST at ARNF and ARSF in 2014

Station name	Lon (°E), Lat (°N)	SVF	EXP_name	SSR MBE (W•m^{-2})	SSR RMSE (W•m^{-2})	SSR *R*	LST MBE (°C)	LST RMSE (°C)	LST R
ARSF	100.52	0.929	Default_SExp	40.68	153.49	0.88	−3.85	5.78	0.84
	38.09		STRE_SExp	22.21	146.30	0.89	−4.27	5.63	0.85
ARNF	100.41	0.875	Default_SExp	38.04	146.83	0.90	2.66	6.90	0.74
	37.98		STRE_SExp	23.58	136.64	0.93	−1.29	4.15	0.87

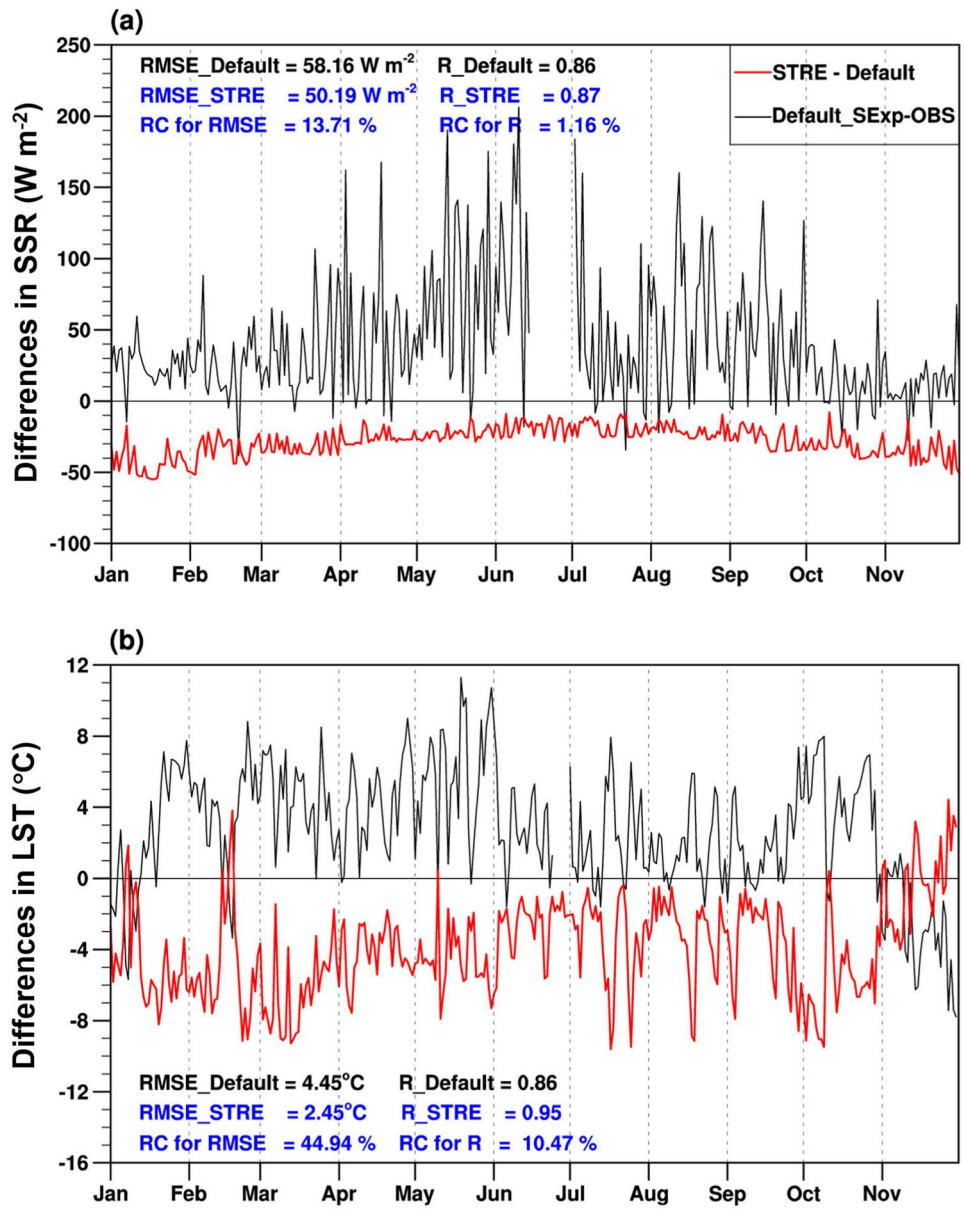

Figure 6. The time series of differences between the modeled and observed daily SSR and LST in 2014 at ARNF with the RMSE, *R* and their relative changes (RC) listed upon.

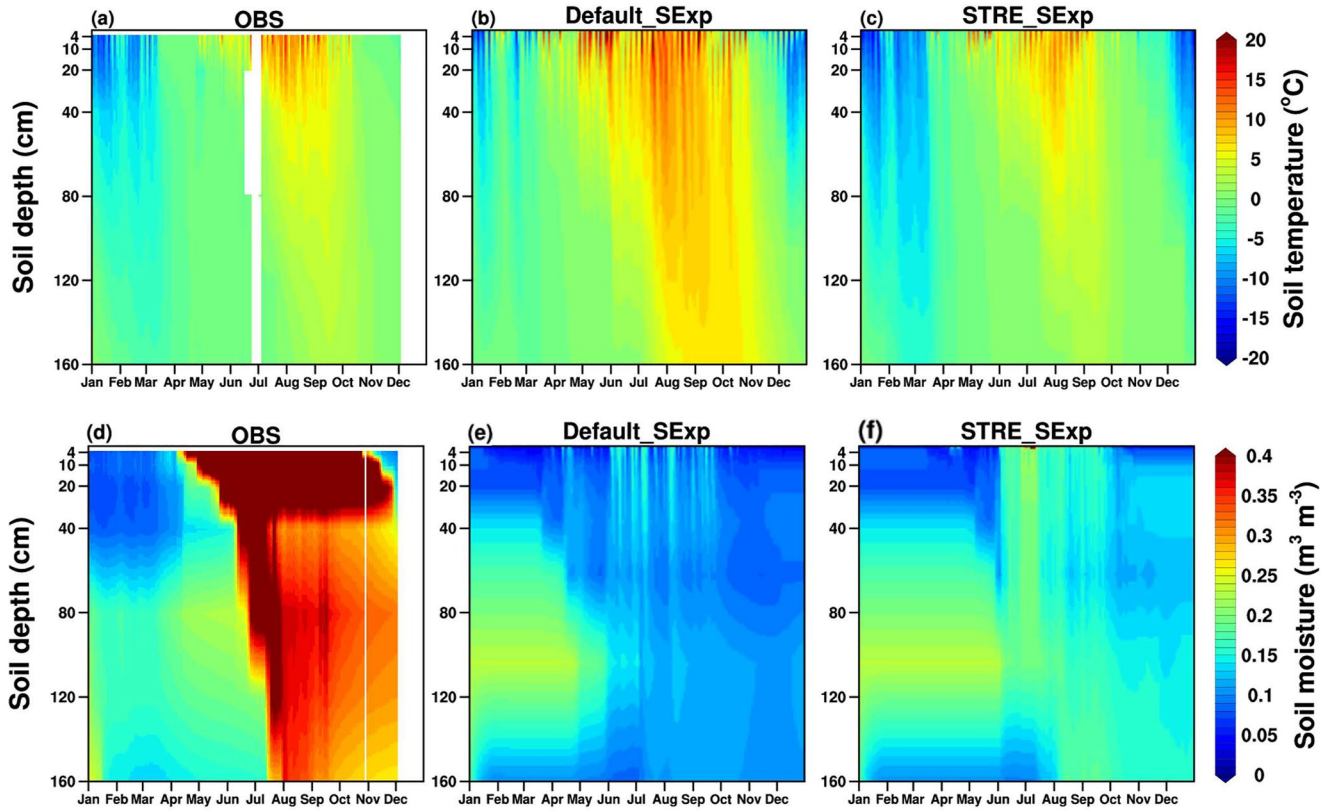

Figure 7. (a–c) The temporal variations of the observed (OBS) and simulated (Default_SExp and STRE_SExp) hourly soil temperature and (d–f) soil moisture vertical profile at ARNF during 2014.

Figure 7 shows the time-depth distribution of observed and simulated soil temperature and moisture at ARNF during 2014. From the observation shown in Figure 7a, the soil temperature increases with the depth during cold season (i.e., November to December and January to April) stratified by a cold upper layer of 0–40 cm and a warm lower layer and decreases with the depth during warm season (i.e., May to October) characterized by a warm upper layer of 0–40 cm and a cool lower layer. The soil at ARNF generally experiences a negative thermal stratification in cold season and positive thermal stratification in warm season every year, the soil temperature at the upper layers in the cold (warm) season gradually decrease due to the heat losses (enhanced heating because of the strengthened solar radiation) at the surface. The soil temperature tends to display an annual minimum (maximum) at different depths in January (August) and show much larger annual variation in the upper layers than in the lower layers. Both experiments can reproduce the time-depth distribution of the soil temperature, however, the Default_SExp tends to overestimate the soil temperature at different depth (Figure 7b) due to the overestimated SSR, which can be significantly reduced by adopting the 3D STRE scheme in CoLM (Figure 6a and Table 1), as a result, the STRE_SExp obviously improves the simulation of the time-depth distribution of soil temperature at each depth (Figure 7c). Compared with the Default_SExp, the STRE_SExp obviously reduces the warm bias due to absorbing more solar radiation by more than 4°C in summer and acceptably reproduces the temporal variation of soil temperature at ARNF.

As we can see from Figure 7d, the observed soil moisture shows rather stable stratification due to the frozen ground during the cold season (i.e., January to March) that the volumetric liquid soil water content gradually becomes larger with the increase of depth and then stabilizes at approximately 0.15 $m^3\ m^{-3}$ in the deeper layer (80–150 cm). From March to April, soil moisture at all depth increases gently as a result of the ice melting process in soil corresponding to the rising soil temperature shown in Figure 7a. During the warm season (from April to September), the soil water content in the upper layer (0–40 cm) rapidly rises with concentrated precipitation (not shown) leading to a durative high value over 0.4 $m^3\ m^{-3}$, and progressively permeates through deeper layers.

19422466, 2022, 1, Downloaded from https://agupubs.onlinelibrary.wiley.com/doi/10.1029/2021MS002654 by Anning Huang , Wiley Online Library on [22/03/2023]. See the Terms and Conditions (https://onlinelibrary.wiley.com/terms-and-conditions) on Wiley Online Library for rules of use; OA articles are governed by the applicable Creative Commons License

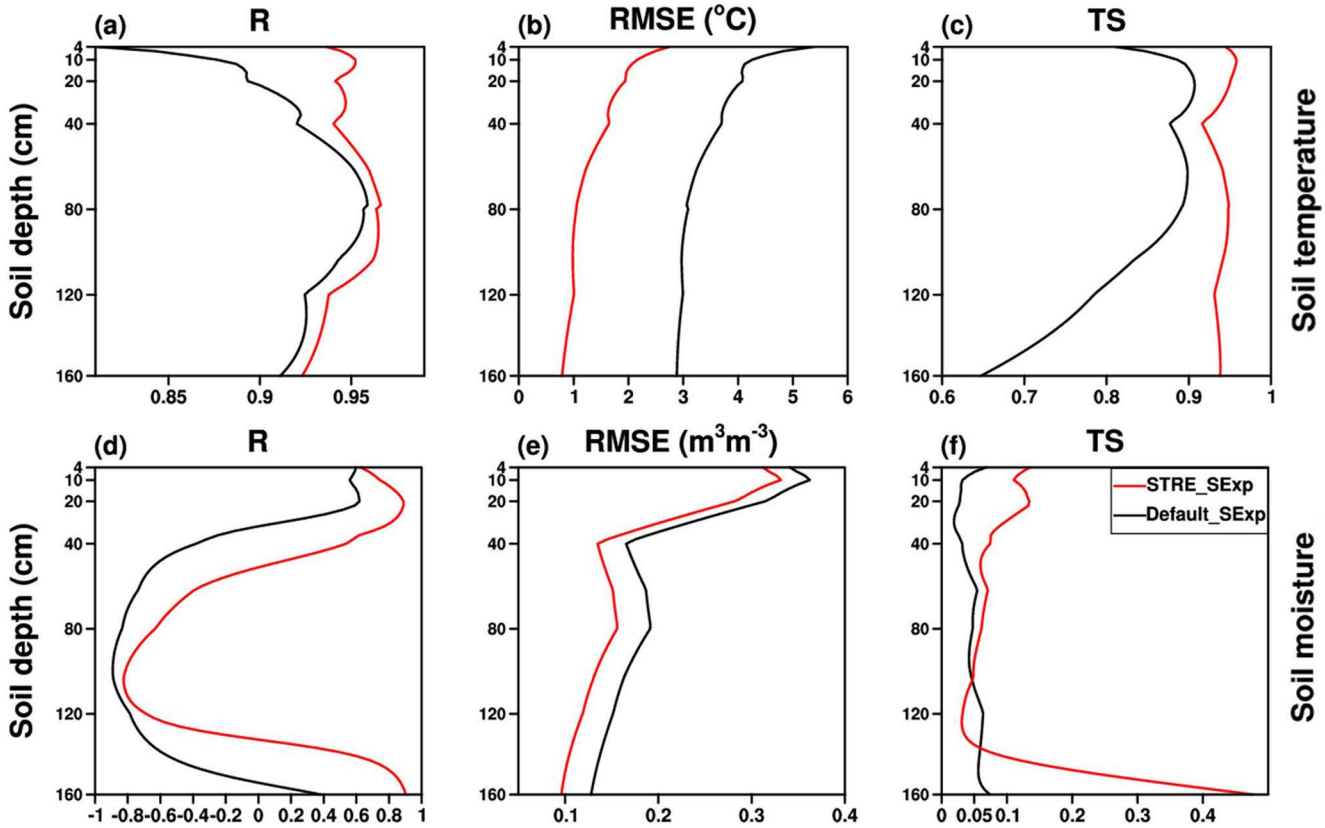

Figure 8. (a–c) The vertical distribution of the temporal correlation coefficient (*R*), root-mean-square error (RMSE), and Taylor score (TS) for the simulated hourly soil temperature and (d–f) moisture against the site observation over 2014.

When ground temperature once again falls below 0°C in the late October, the soil moisture at the upper layer quickly responds and declines under 0.1 m^3m^{-3}.

The soil moisture simulation is well known to be highly sensitive to the soil hydraulic parameters such as porosity, saturated hydraulic conductivity and fractions of sand, silt, and clay (Rieu & Sposito, 1991). If calibration was not performed, these soil parameters are set according to original datasets included in CoLM, which may differ so much from actual soil properties on site that significant model errors will occur. For example, in CoLM model, the soil porosity at ARNF remain unchanged from 0.215 to 0.195 with the soil depth increases, which is unreasonable and could introduce evident deviations into soil moisture simulations since the soil porosity is mutually interacted with the growth condition of the plant roots (Laio et al., 2006) and is obviously time-varying. Apart from the precipitation distribution and soil hydraulic parameters, the terrain slope and aspect can also explain the continuous large liquid soil water content in the ARNF station that a slope of 13.81°drives the water content from the top of the hill gradually seeping to the lower area and a shady and north-faced hillside undermines the surface evapotranspiration due to the reduced SSR. Although both simulation experiments strongly underestimate the soil moisture in summer (Figures 7d and 7f), the inclusion of 3D STRE scheme does show improvement in diminishing bias by over 0.1 m^3 m^{-3} through reducing the evapotranspiration of surface soil water content with calibration of the overestimated SSR.

To quantify the performance of these two experiments in simulating the soil temperature and moisture at different depths, Figure 8 further gives the vertical distribution of the *R*, RMSE, and TS values for the hourly soil temperature and moisture simulated by Default_SExp and STRE_SExp against the observation, respectively. From Figure 8a, the *R* values of soil temperature produced by the STRE_SExp ranging from 0.92 to 0.97 are higher than that in the Default_SExp at all depths. Especially in the upper soil layer (0–40 cm), the STRE_SExp shows obviously higher *R* values than the Default_SExp by averagely over 0.05, suggesting that the temporal variation of soil temperature at surface layer is strongly influenced by the less SSR due to topographic shading effects and

19422466, 2022, 1, Downloaded from https://agupubs.onlinelibrary.wiley.com/doi/10.1029/2021MS002654 by Anning Huang , Wiley Online Library on [22/03/2023]. See the Terms and Conditions (https://onlinelibrary.wiley.com/terms-and-conditions) on Wiley Online Library for rules of use; OA articles are governed by the applicable Creative Commons License

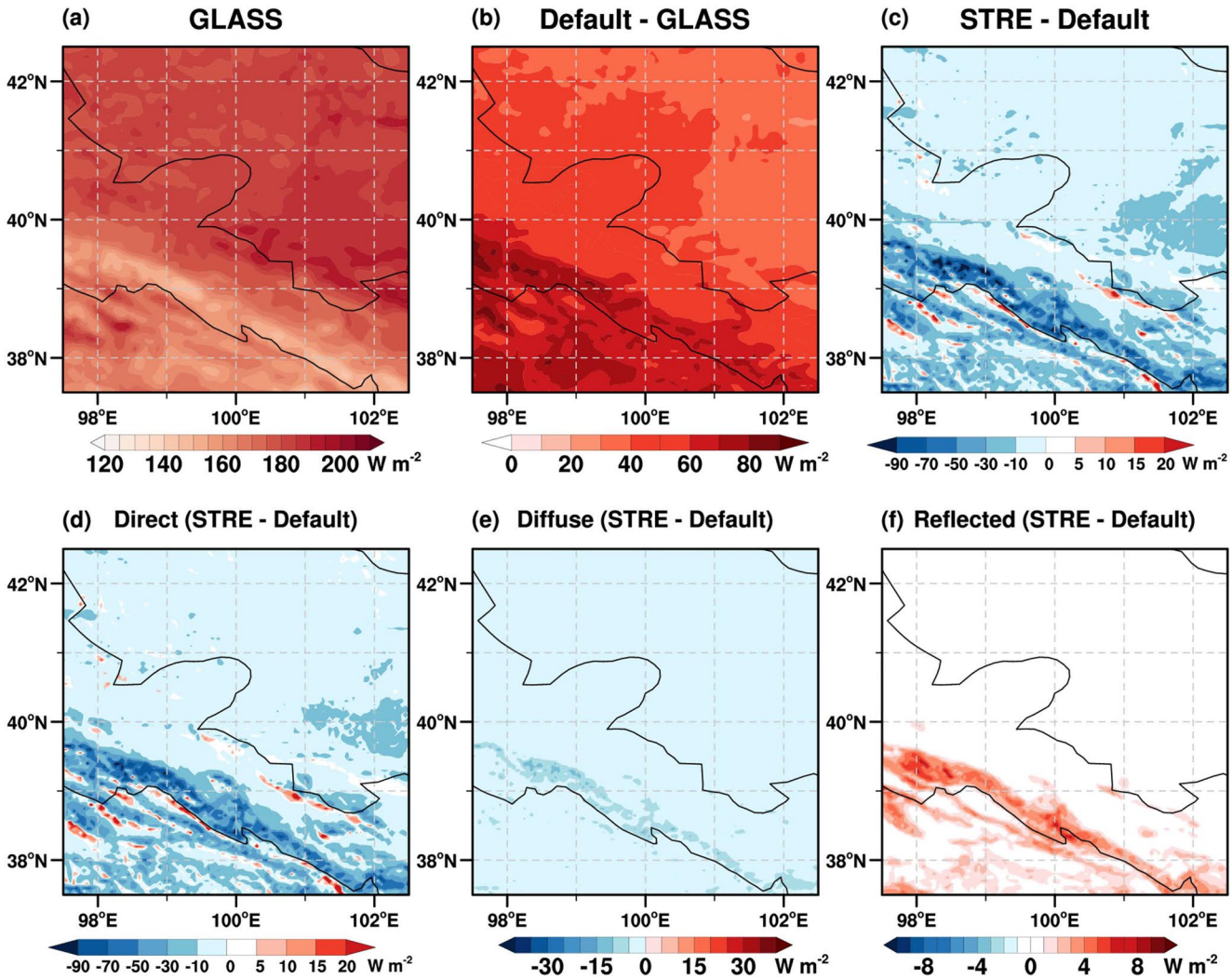

Figure 9. The annual mean SSR from (a) GLASS and SSR differences (b) between GLASS and the Default_RExp, and (c) between GLASS and the STRE_RExp from 2013 to 2015, as well as the deviations in direct radiation (d), (e) diffuse radiation and (f) terrain reflected radiation between STRE_RExp and Default_RExp.

is consequently in more consistent with the observation. Meanwhile, the STRE_SExp shows better ability in simulating the soil temperature magnitude than the Default_SExp with the RMSE values decreased by approximately 2°C at all depths (Figure 8b). Correspondingly, the model performance in simulating the amplitude and pattern of the soil temperature variability (Figure 8c) is remarkably improved in consideration of the 3D STRE scheme with all the TS values more than 0.9, particularly in deeper layers (100–160 cm). As to the soil moisture simulation, the STRE_SExp still exhibits advantages that the RMSE (R and TS) values are relatively lower (higher) at most depths compared to the Default_SExp (Figures 8d–8f).

3.2. Validation of the Regional Simulation

Figures 9a–9c display the annual mean SSR from GLASS and the SSR differences between Default_RExp and GLASS, and between STRE_RExp and Default_RExp, respectively. The spatial distribution of SSR in the GLASS product is consistent with the pattern of elevation map, while the Default_RExp shows large discrepancies in valley areas along the Qilian Mountains, which can exceed ~50 W m^{-2} (Figure 9b). With the inclusion of the 3D STRE scheme, the overestimation of SSR in the Default_RExp can be substantially diminished over rugged terrains (Figure 9c) so that the domain averaged MBE decreases from 50.4 W m^{-2} to 34.7 W m^{-2} (improved by 31.2%), and the domain averaged RMSE declines from 52.1 W m^{-2} to 38.6 W m^{-2} (improved by 25.9%) simultaneously. The shading effects induced by the parameter SF on direct radiation (Figure 9d) can primarily explain

19422466, 2022, 1, Downloaded from https://agupubs.onlinelibrary.wiley.com/doi/10.1029/2021MS002654 by Anming Huang , Wiley Online Library on [22/03/2023]. See the Terms and Conditions (https://onlinelibrary.wiley.com/terms-and-conditions) on Wiley Online Library for rules of use; OA articles are governed by the applicable Creative Commons License

19422466, 2022, 1, Downloaded from https://agupubs.onlinelibrary.wiley.com/doi/10.1029/2021MS002654 by Anning Huang , Wiley Online Library on [22/03/2023]. See the Terms and Conditions (https://onlinelibrary.wiley.com/terms-and-conditions) on Wiley Online Library for rules of use; OA articles are governed by the applicable Creative Commons License

this improvement in valley areas along the Qilian Mountains, while the diffuse radiation and reflected radiation from surrounding terrain contribute slightly to the improved SSR (Figures 9e and 9f).

The impact of the 3D STRE scheme on radiation field at the surface will further affect the surface energy balance processes:

$$NR = SH + LH + GH \tag{23}$$

where NR is the net radiation including surface net solar radiation flux (NSW) and net longwave radiation flux (NLW), SH, and LH represent the sensible heat flux and latent heat flux respectively, and GH denotes the soil heat flux. Here, the NSW, NR = NSW-NLW and GH are positive downward at the surface, while the NLW, SH, and LH are positive upward. Figure 10 displays the spatial pattern of induced changes for these surface heat fluxes between two experiments (STRE_RExp - Default_RExp). In addition, to quantify the influence of the 3D STRE scheme, domain averaged differences and relative differences of NSW, NLW, NR, SH, LH, and GH are illustrated in Figure 11. We found that the spatial pattern and magnitude of differences for NSW and NR (Figures 10a and 10c) are highly congruent that they both show minimums below -80 W m^{-2} at valley areas around Qilian Mountains, while the differences in NLW are much smaller than that of shortwave flux changes. Differences in SH (Figure 10d) range between -60 and 5 W m^{-2} are much larger than those of LH and GH, indicating that the majority of changes in surface solar fluxes is compensated by the reduction of SH (Figure 11a) due to the decreasing ground-air temperature gradient. A detailed evaluation for influences of the 3D STRE scheme on the evapotranspiration (not shown) shows consistency with the pattern of differences in LH (Figure 10e). Compared with the Default_RExp, the STRE_RExp undermines the overestimated evapotranspiration in mountainous areas through reducing the absorbed SSR, implying that much moist alpine areas will occur along the Qilian Mountains after implementing the 3D STRE scheme. This conclusion is confirmed by the following analysis of soil moisture simulation results against with the ground measurements. The differences in GH are noticeably smaller with a regional mean value of -0.02 W m^{-2} and statistically insignificant in annual mean.

As shown in Figure 11, with the consideration of sub-grid terrain effects, the surface NR is reduced by 9.57 W m^{-2} (relative change of 14.01%) with the NSW (NLW) decreased by 12.36 W m^{-2} (2.78 W m^{-2}). Consequently, the sum of SH, LH and GH declined by 9.93 W m^{-2} (relative change of 14.08%) to compensate the reduction of the NR, in which the reduction of sensible heat flux (8.94 W m^{-2}) accounts for the most, while the decrease in latent heat flux (1.01 W m^{-2}) is less prominent. The primary reason why the changes in NR cannot be strictly equal to the sum of other surface heat flux is that the CoLM has included the parameterization of heat flux from precipitation to the ground in the energy balance process at soil surface.

The effect of the 3D STRE on CoLM in simulating the seasonal variations of LST is shown in Figure 12 and quantitative analysis with RMSE and TS values for each experiment against the observation and their percentage changes produced by the STRE_RExp relative to the Default_RExp are illustrated in Figure 13. Generally, the spatial pattern of LST in the observation shows an increasing trend from south to north in the whole year, basically following the spatial pattern of the NR (Figure 10c). Compared to the observation, the Default_RExp underestimates the LST over the most part of the northern region of the Heihe River Basin all year round, especially over the Badain Jaran Desert, while positive biases are only located in valleys along the Qilian Mountains with an annual mean RMSE value of 3.75°C and an annual mean TS value of 0.976 (Figures 13a and 13c). Moreover, the Default_RExp shows relative larger negative deviations in winter and spring by over 4°C at the southern part of the study area with the elevation over 4,000 m (Figure 1a, mostly in Qinghai province) than those in summer and autumn, suggesting that the model performance is not good enough in snow cover simulation, so that the RMSE value in winter is the highest for 4.79°C, followed by 4.19°C in spring (Figure 13a). Inclusion of the 3D STRE scheme, the STRE_RExp exhibits an expected improvement in simulating the LST in mountainous regions that negative discrepancies between the STRE_RExp and Default_RExp exactly compensate the overestimation of the Default_RExp in the valleys along the Qilian Mountains, leading to remarkable reductions in RMSE values for all seasons (Figures 13a and 13b). The RMSE in winter depresses the most by 0.98°C (improved by 20.46%), while the reduction in summer is less prominent for 0.24°C (accounting for 7.02%) since the shadow casting effects become much stronger (weaker) due to relatively smaller (larger) solar zenith angles in cold (warm) seasons (Hao et al., 2018). Corresponding to this, comparatively observable increase in TS values are shown in Figure 13d during autumn (improved by 4.78%) and winter (improved by 5.68%).

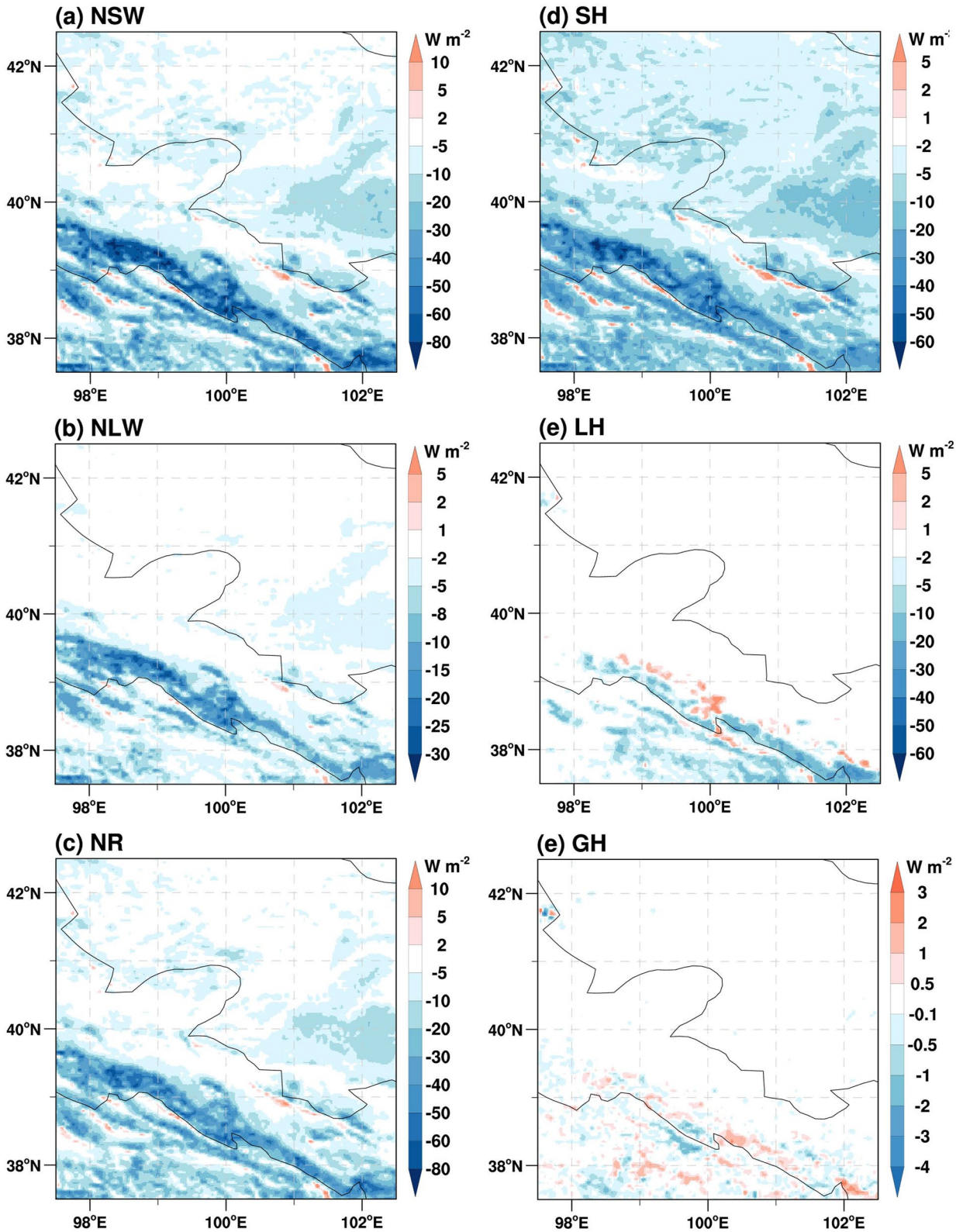

Figure 10. The differences in each component of surface heat balance averaged over 2013–2015 between STRE_RExp and Default_RExp. (a) Net solar radiation flux, (b) net longwave radiation flux, (c) net radiation flux, (d) sensible heat flux, (e) latent heat flux, and (g) ground heat flux.

19422466, 2022, 1, Downloaded from https://agupubs.onlinelibrary.wiley.com/doi/10.1029/2021MS002654 by Anning Huang , Wiley Online Library on [22/03/2023]. See the Terms and Conditions (https://onlinelibrary.wiley.com/terms-and-conditions) on Wiley Online Library for rules of use; OA articles are governed by the applicable Creative Commons License

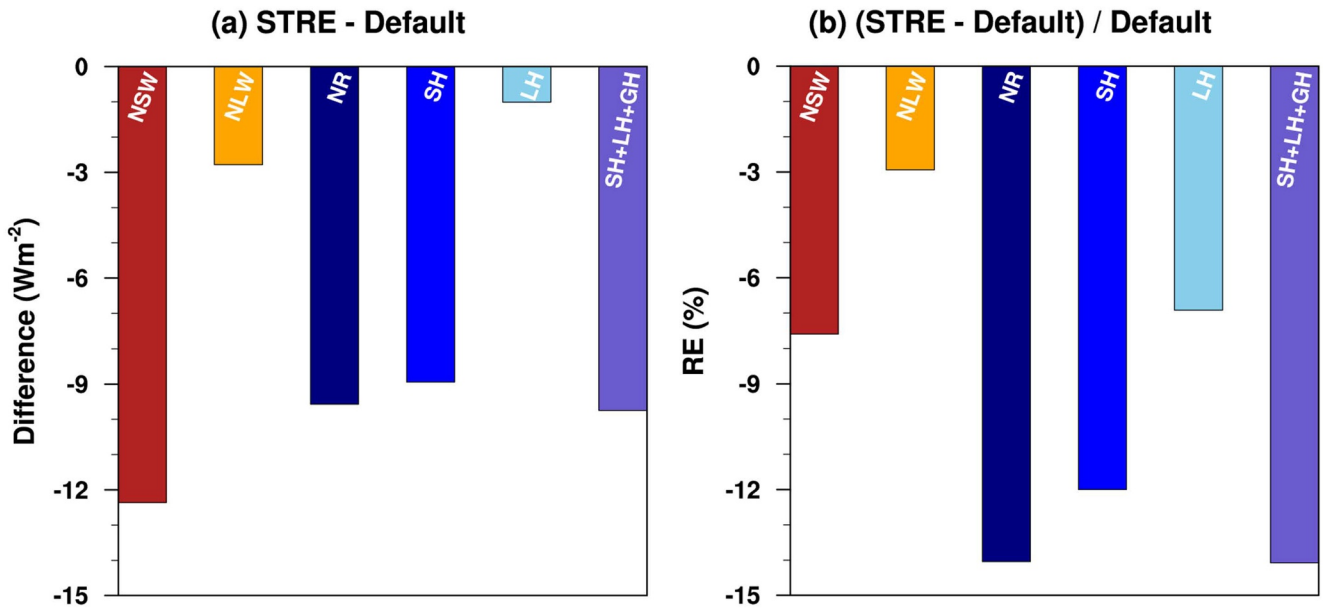

Figure 11. (a) The regional mean differences and (b) relative differences in the surface radiation and heat fluxes between STRE_RExp and Default_RExp averaged over 2013–2015.

Figures 14 and 15 separately demonstrate the percentage changes of TS and RMSE values (STRE_RExp minus Default_RExp divided by Default_RExp, positive [negative] values in Figures 14 and 15) represent the improvement by using the 3D STRE scheme for the daily simulated soil temperature and moisture at the depth of 4 and 20 cm of 37 WSN nodes over the upper branch of the Heihe River Basin. In general, the STRE_RExp performs better than the Default_RExp with more than 80% of WSN nodes showing positive changes in TS for both soil temperature and moisture simulations. Regarding the soil temperature simulation, responding to the adjustment in SSR, the TS values produced by the STRE_RExp (Figures 14a and 14b) are improved by 3.7% (3.6%) while the RMSE values (Figures 15a and 15b) are decreased by 5.2% (1.5%) at the depth of 4 (20) cm on average, especially at the WSN nodes situated on the north-faced slope which are severely obstructed by surrounding topography with obviously lower SVF values. Figures 14c, 14d, 15c, and 15d reveal that the inclusion of the STRE scheme can substantially improve the soil moisture simulation with the average TS increased by 14.0% (14.3%) and the average RMSE declined by 3.9% (1.7%) at the depth of 4 (20) cm compared to the Default_RExp.

Overall, the results are acceptable for two reasons. First, the scale mismatch between field observations and model simulation would be introduced during spatial interpolation by using the inverse distant weighted method. Second, the 3D STRE scheme essentially calculates an area average of SSR in a model pixel which inevitably leading to a lower spatial heterogeneity. With a horizontal resolution of 5 km in this study, discrepancies caused by smoothed topographic shading effects would limit the accuracy of surface energy balance estimates as well as soil parameters simulations.

4. Discussion

We proposed a 3D STRE scheme that using the regionally averaged sub-grid topographic factors on each model grid, which can be pre-calculated based on high-resolution DEM data, to parameterize the sub-grid topographic effects on SSR. In particular, we developed a fast table-lookup method for computing the time-variant shading factor (SF) to avoid vast data processing during integration time by pre-computing the distribution of the sine values of the maximum terrain shading elevation angle ($\sin(\varepsilon_{\phi_{k,i}})_{\max}$), which could save approximately 60.75% computation time for model integration. The physically realistic superiority of the 3D STRE scheme is also shown by comparing the parameterized solar radiation fluxes with the modeled clear-sky solar radiation fluxes, which derived by area-averaging the explicitly calculated sub-grid radiation fluxes to model grid scale. The parameterized SSR in January 2014 (not shown) displays good agreement with the modeled solar radiation in terms of both

19422466, 2022, 1, Downloaded from https://agupubs.onlinelibrary.wiley.com/doi/10.1029/2021MS002654 by Anning Huang , Wiley Online Library on [22/03/2023]. See the Terms and Conditions (https://onlinelibrary.wiley.com/terms-and-conditions) on Wiley Online Library for rules of use; OA articles are governed by the applicable Creative Commons License

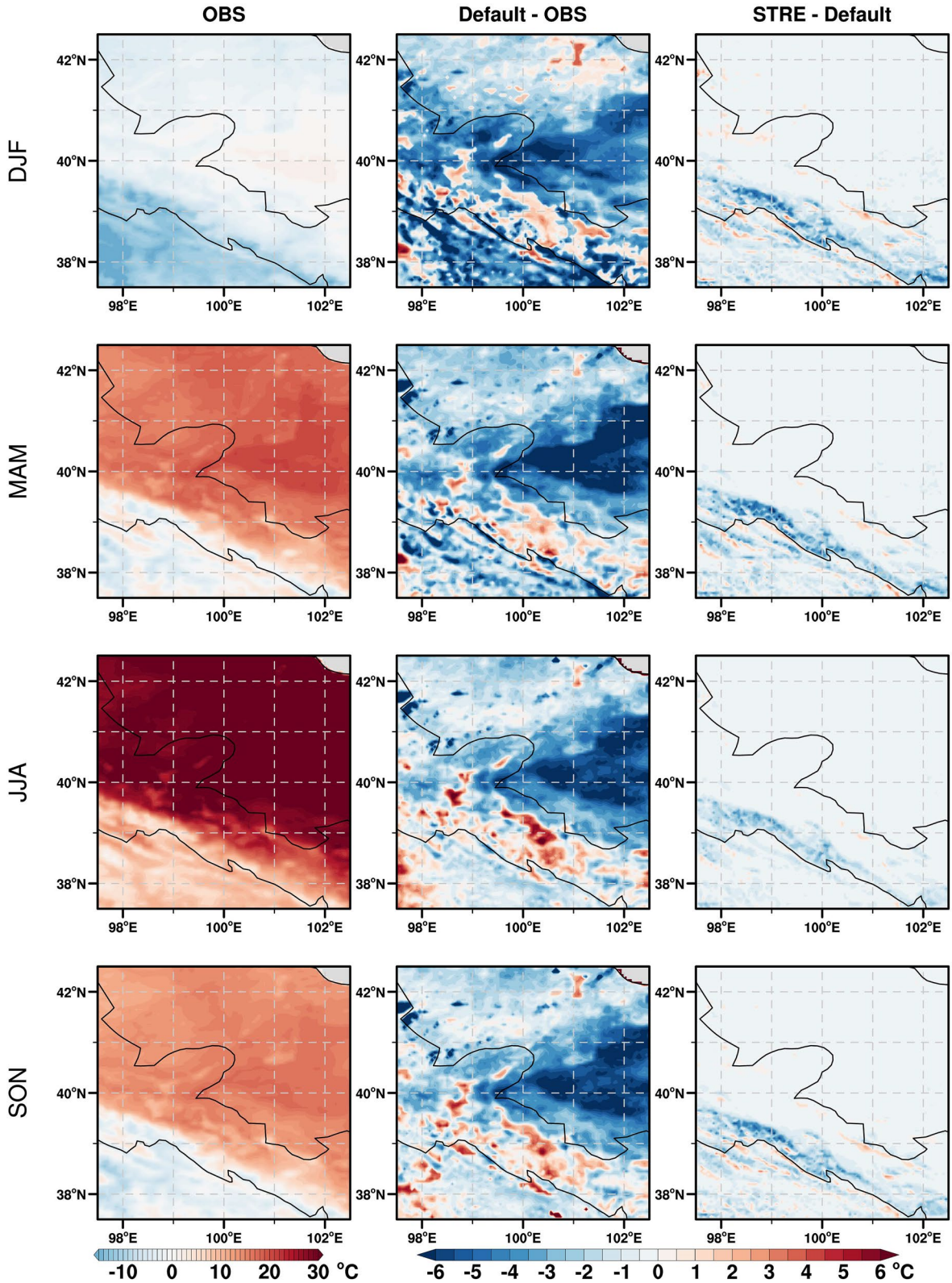

Figure 12. Spatial distributions of the observed LST (left column) and the LST differences between the Default_RExp and observation (middle column), and between STRE_RExp and Default_RExp (right column) in different seasons averaged over 2013–2015.

19422466, 2022, 1, Downloaded from https://agupubs.onlinelibrary.wiley.com/doi/10.1029/2021MS002654 by Anning Huang , Wiley Online Library on [22/03/2023]. See the Terms and Conditions (https://onlinelibrary.wiley.com/terms-and-conditions) on Wiley Online Library for rules of use; OA articles are governed by the applicable Creative Commons License

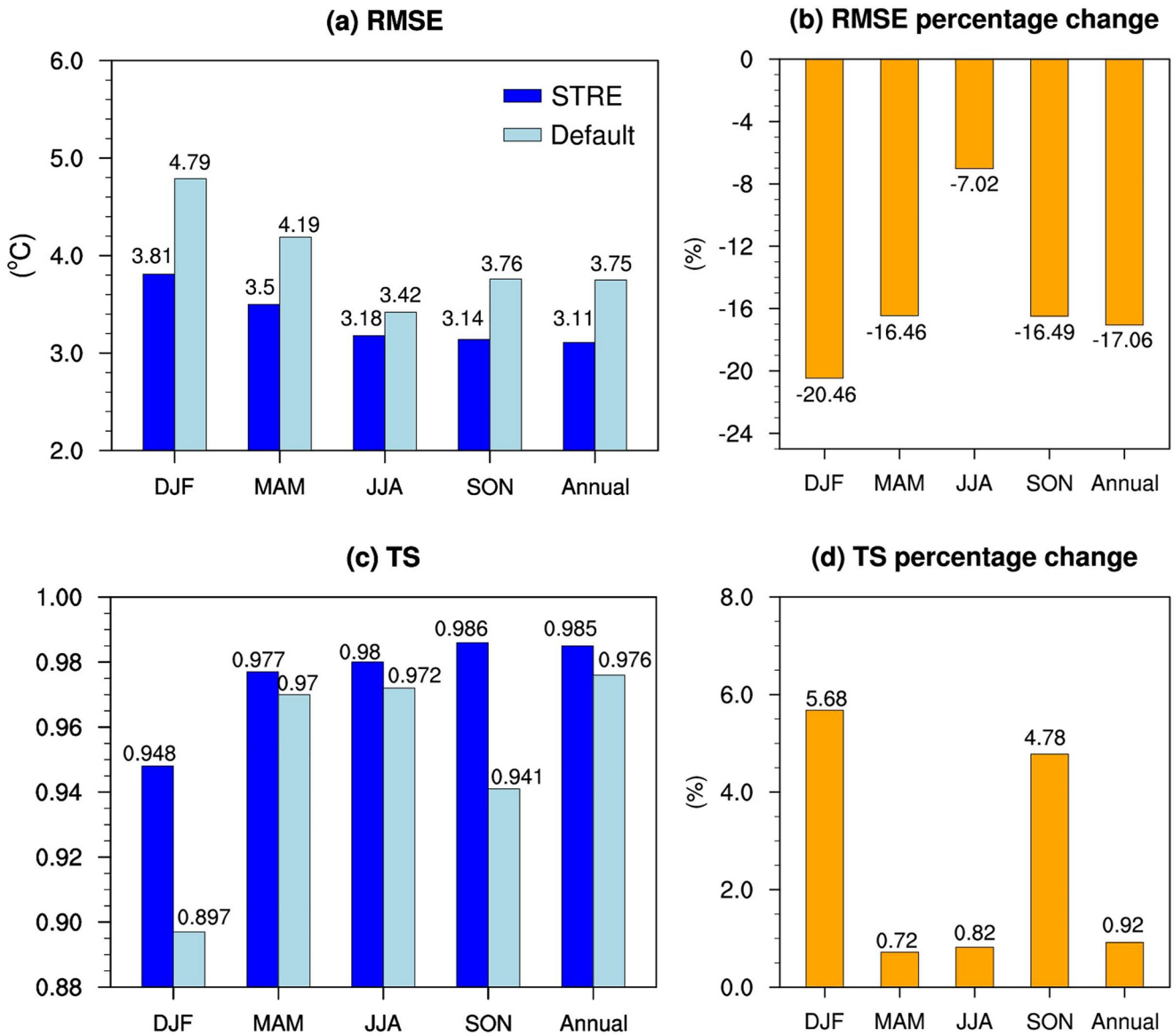

Figure 13. (a) The root-mean-square errors and (c) Taylor scores of the seasonal and annual mean LST simulated by Default-RExp and STRE-RExp against the observation over 2013–2015 and (b and d) their percentage changes produced by the STRE_RExp relative to the Default_RExp.

diurnal and spatial variations in mountain regions. The 3D STRE scheme only leads to minor deviations (within ± 20 W m^{-2}) in daily mean SSR with a reasonably high TS value of 0.99 compared to the explicit calculations.

Overall, the 3D STRE scheme can offer the CoLM more realistic representation of surface radiation process and significantly improve soil temperature and moisture simulations over the areas with complex terrain. However, there are still some limitations in the 3D STRE scheme, that is, the accuracy of the SVF and SF calculations is largely dependent on the maximum research radius (R), the number (N) of distributed azimuth angles and the number (M) of discretized solar elevation angles. During the pre-calculating process, the larger R, N and M we choose, the more time-consuming loop calculation and heavier storage burden we have. For example, when setting $N = 240$ and $M = 100$, the calculation of the assemble of $\sin(\epsilon_{\phi_{k,i}})_{\max}$ with the search radius setting for 4.5 km spent 3.79 hr, while the calculation with the search radius setting for 9 km spent 5.09 hr. Every time the search radius increased by 0.9 km, the calculation time increased by approximately 0.21 hr. Taking account of the balance between the high accuracy of parameters for the 3D STRE scheme with the minimization of computational demand, the setup of R, N and M should be determined though carrying out large amount of sensitivity

19422466, 2022, 1, Downloaded from https://agupubs.onlinelibrary.wiley.com/doi/10.1029/2021MS002654 by Anning Huang , Wiley Online Library on [22/03/2023]. See the Terms and Conditions (https://onlinelibrary.wiley.com/terms-and-conditions) on Wiley Online Library for rules of use; OA articles are governed by the applicable Creative Commons License

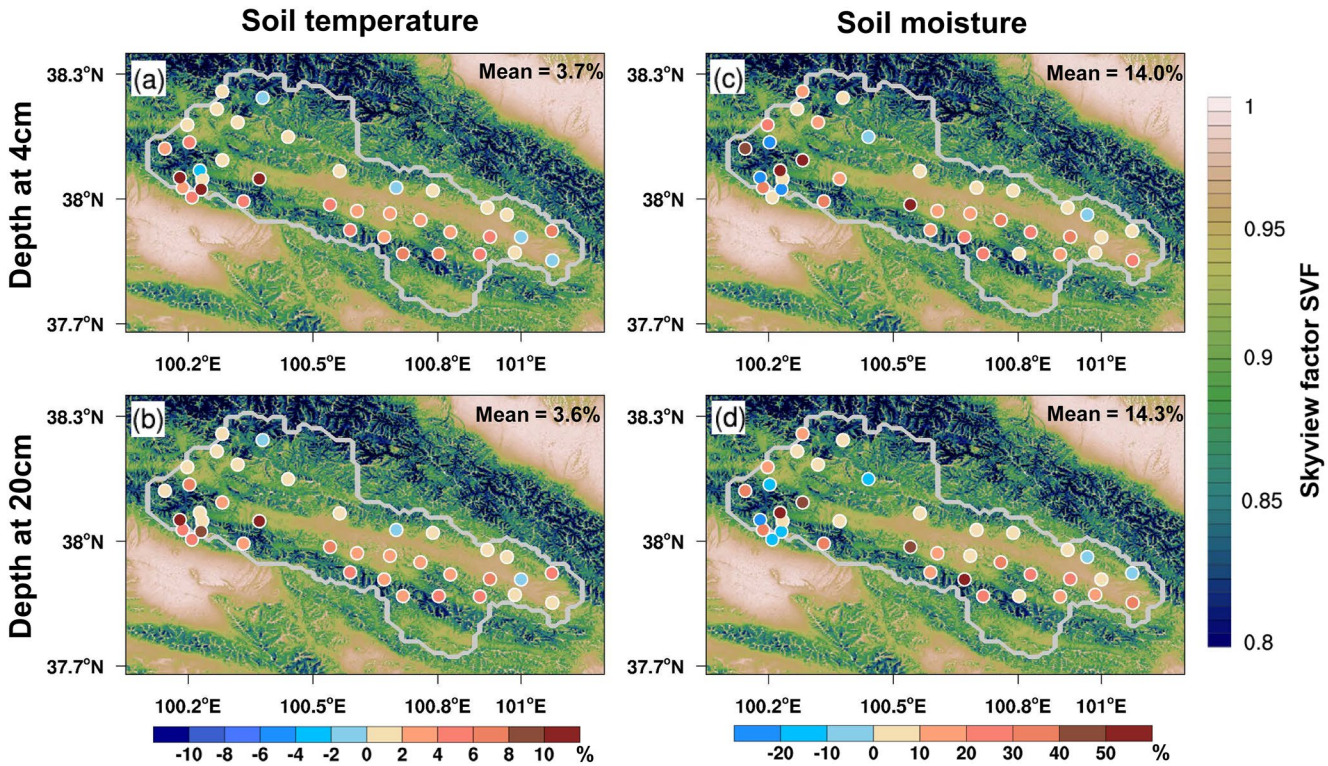

Figure 14. Percentage changes of TS values for the soil temperature and moisture at the depths of 4 and 20 cm produced by the STRE_RExp relative to those produced by the Default_RExp across the 37 WSN nodes during 2014. The averaged improvements in TS values (Mean) are listed upon at the top right-hand corner of each sub-figure.

experiments. Furthermore, in the parameterization of direct SSR (Equation 14), we simplified the calculation of $(SF\cos\gamma)_p$ into $SF_p(\cos\gamma)_p$ by omitting the nonlinear cross terms introduced by $SF_i(\cos\gamma)_i$, such approximation may lead to errors for SSR simulation in highly anisotropic topographies, especially when the solar elevation angle becomes smaller with the SF_i and $(\cos\gamma)_i$ approaching to zero. The complicated parameterization of cross terms in $(SF\cos\gamma)_p$ need further discussion to refine the representations of SSR in complex terrain.

In addition, the hydrological processes such as subsurface flows and lateral surface flows, which are strongly dependent on the topography and are not elaborately described, may play an important role in simulating evapotranspiration and soil water content profiles at hill-slope scale (Chang et al., 2018; Ji et al., 2017). Many researchers have developed a variety of quasi 3D models through coupling the lateral flow in saturated zones with the vertical flow in the unsaturated sections (e.g., Hazenberg et al., 2015; Shen & Phanikumar, 2010). Besides, topographic variables can clearly affect plant species distributions in mountainous environments (Hwang et al., 2011; Kayiranga et al., 2017; Wood et al., 2011) through changing microclimate (e.g., precipitation, solar radiation received by canopy), which in turn strongly influenced the heat, water and CO_2 exchange between the atmosphere and land surface, suggesting that interactions between sub-grid topography and vegetation types should be taken into account to promote the potential of CoLM model simulations.

The strong spatial variability of SSR distribution will further contribute to heterogeneous land surface fluxes, which could exert substantial influences on the mixing processes and vertical structures at the atmospheric boundary layer (C. M. Wu et al., 2015). Moreover, the simulation ability of air temperature and precipitation in climate models can be refined through supplementing comprehensive feedback mechanisms induced by the 3D STRE scheme into the representation of land-air interactions (G. Y. Chen et al., 2019; C. Gu et al., 2020), which also provide an important insight into complementing deficiencies in reproducing precipitation over Tibet Plateau for different numerical models, especially overestimated precipitation in the southern TP and mendacious precipitation center, apart from adding sub-grid orographic drag effects (Jimenez & Dudhia, 2013; X. J. Wang et al., 2018; Zhu et al., 2018).

19422466, 2022, 1, Downloaded from https://agupubs.onlinelibrary.wiley.com/doi/10.1029/2021MS002654 by Anning Huang , Wiley Online Library on [22/03/2023]. See the Terms and Conditions (https://onlinelibrary.wiley.com/terms-and-conditions) on Wiley Online Library for rules of use; OA articles are governed by the applicable Creative Commons License

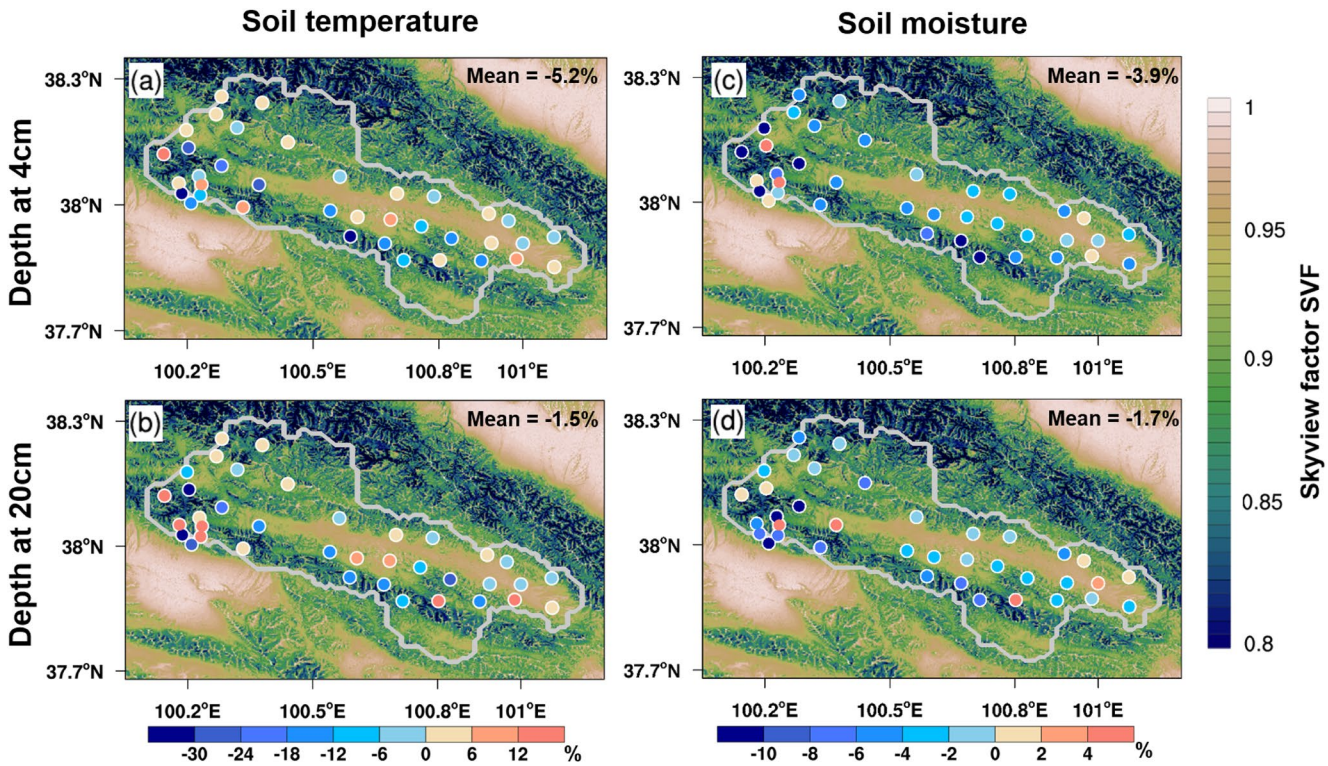

Figure 15. Percentage changes of RMSE values for the soil temperature and moisture at the depths of 4 and 20 cm produced by the STRE_RExp relative to those produced by the Default_RExp across the 37 WSN nodes during 2014. The averaged improvements in RMSE values (Mean) are listed upon at the top right-hand corner of each sub-figure.

Although the STRE effects on solar radiation are more important at finer spatial resolutions, they cannot be simply neglected at coarse spatial scales (Nian, 2020). It indicates that the STRE influences on surface energy balance, surface temperature and snow cover are still significant even at the spatial resolution as low as around 2° (Hao et al., 2021). As a critical physical process that has not been widely incorporated in most current land surface models, further studies are planned for coupling with an appropriate climate model with different model resolutions to investigate the long-term 3D STRE influences over mountainous areas in the TP, especially its impact on the noteworthy thermal and hydrological processes like snow melting and evapotranspiration.

5. Conclusions

In this study, we developed a 3D STRE scheme with much more realistic description of SSR and implemented it into the CoLM to enhance the description of surface radiation process over complex terrains and investigated its impact on simulation of soil temperature and moisture and surface energy budget over Heihe River Basin in China. Results show that the CoLM coupled with 3D STRE scheme obviously improves the simulations of soil thermal and moist features at both single-point and regional scales. The main findings are summarized as follows:

Compared to the Default_SExp without 3D STRE scheme, the performance of single-point simulations from the STRE_SExp using the CoLM with 3D STRE scheme shows better consistencies with the observed SSR and LST data in ARNF station, the RMSE of the estimated LST is significantly reduced by ~45% with its temporal correlation increased by ~10.5%, resulted from the RMSE of simulated SSR reduced by ~13.7%. Consequently, the simulation of soil temperature and moisture vertical profile in the STRE_SExp is obviously in more accordance with the field measurements at most depths in terms of RMSE and TS relative to Default_SExp.

Further evaluation of the influence of 3D STRE scheme on the spatial distribution of SSR simulation by carrying out regional simulation over Heihe River Basin indicates that inclusion of the 3D STRE scheme reduces the substantial overestimation of SSR in valley areas, mostly due to the shading effect for direct radiation with the MBE (RMSE) decreased by 31.2% (25.9%) relative to the simulations without considering the 3D STRE.

19422466, 2022, 1, Downloaded from https://agupubs.onlinelibrary.wiley.com/doi/10.1029/2021MS002654 by Anning Huang , Wiley Online Library on [22/03/2023]. See the Terms and Conditions (https://onlinelibrary.wiley.com/terms-and-conditions) on Wiley Online Library for rules of use; OA articles are governed by the applicable Creative Commons License

19422466, 2022, 1, Downloaded from https://agupubs.onlinelibrary.wiley.com/doi/10.1029/2021MS002654 by Anning Huang , Wiley Online Library on [22/03/2023]. See the Terms and Conditions (https://onlinelibrary.wiley.com/terms-and-conditions) on Wiley Online Library for rules of use; OA articles are governed by the applicable Creative Commons License

As a result, the representations of surface energy balance in mountainous regions also make adjustments with the implementation of 3D STRE scheme that the reduction of the NR is mostly compensated by the decrease in sensible heat flux.

Corresponding to the redistribution of surface heat fluxes, the STRE_RExp experiment further reduces the RMSE of LST simulation by 17.06% for all seasons relative to the Default_RExp on account of its out-performance in valley areas. The simulated soil temperature and soil moisture are also in reasonably agreement with the field observations at 37 WSN nodes in the upper reach of Heihe River Basin in consideration of 3D STRE effects that over 80% of WSN nodes show positive changes in TS score for both soil temperature and moisture simulations, especially those WSN nodes situated on the north-faced slope severely shaded by the adjacent terrain. These results emphasize the significance of considering the sub-grid topographical effects on the SSR in land surface modeling and are enormously helpful to promote our understanding and simulation of surface energy exchanges in the regions with complex topography.

Data Availability Statement

The authors sincerely thank National Tibetan Plateau Data Center (http://poles.tpdc.ac.cn), National Earth System Science Data Center, National Science & Technology Infrastructure of China (http://www.geodata.cn), CIAT (http://srtm.csi.cgiar.org) for permitting us to use the data.

Acknowledgments
The authors acknowledge the National Key R&D Program of China under Grant 2017YFA0604301, the National Natural Science Foundation of China under grants 41975081 and 41975130, the CAS "Light of West China" Program, and the Fundamental Research Funds for the Central Universities and the Jiangsu Collaborative Innovation Center for Climate Change to support this study. The authors thank the two anonymous reviewers for the very insightful, constructive and detailed comments to significantly improve the manuscript.

References

Aguilar, C., Herrero, J., & Polo, M. J. (2010). Topographic effects on solar radiation distribution in mountainous watersheds and their influence on reference evapotranspiration estimates at watershed scale. *Hydrology and Earth System Sciences*, *14*(12), 2479–2494. https://doi.org/10.5194/hess-14-2479-2010

Arthur, R. S., Lundquist, K. A., Mirocha, J. D., & Chow, F. K. (2018). Topographic effects on radiation in the WRF model with the immersed boundary method: Implementation, validation, and application to complex terrain. *Monthly Weather Review*, *146*(10), 3277–3292. https://doi.org/10.1175/mwr-d-18-0108.1

Barry, R. G. (1992). *Mountain weather and climate* (3rd ed.). Cambridge University Press. https://doi.org/10.1111/j.1541-0064.2010.00351.x

Bonan, G. B. (1996). *A land surface model (LSM version 1.0) for ecological, hydrological, and atmospheric studies: Technical description and user's guide*. NCAR Technical Note.

Chang, L. L., Dwivedi, R., Knowles, J. F., Fang, Y. H., Niu, G. Y., Pelletier, J. D., et al. (2018). Why do large-scale land surface models produce a low ratio of transpiration to evapotranspiration? *Journal of Geophysical Research: Atmospheres*, *123*(17), 9109–9130. https://doi.org/10.1029/2018jd029159

Che, T., Li, X., Liu, S., Li, H., Xu, Z., Tan, J., et al. (2019). Integrated hydrometeorological, snow and frozen-ground observations in the alpine region of the Heihe River Basin, China. *Earth System Science Data*, *11*(3), 1483–1499. https://doi.org/10.5194/essd-11-1483-2019

Chen, G. Y., Wei, Z. G., Dong, W. J., Zhu, X., Chen, C., Liu, Y. J., & Zhang, Z. J. (2019). Effects of improvement of land surface subgrid topographic parameterization on regional temperature and precipitation simulation in Western China. *Chinese Journal of Atmospheric Sciences*, *43*(4), 846–860. https://doi.org/10.3878/j.issn.1006-9895.1807.18156

Chen, L., Yan, G., Wang, T., Ren, H., Calbo, J., Zhao, J., & McKenzie, R. (2012). Estimation of surface shortwave radiation components under all sky conditions: Modeling and sensitivity analysis. *Remote Sensing of Environment*, *123*, 457–469. https://doi.org/10.1016/j.rse.2012.04.006

Chen, Y., Hall, A., & Liou, K. N. (2006). Application of three-dimensional solar radiative transfer to mountains. *Journal of Geophysical Research*, *111*(D21). https://doi.org/10.1029/2006jd007163

Chen, Y., & Liou, K. N. (2006). A Monte Carlo method for 3D thermal infrared radiative transfer. *Journal of Quantitative Spectroscopy & Radiative Transfer*, *101*(1), 166–178. https://doi.org/10.1016/j.jqsrt.2005.10.002

Cheng, G. D., Li, X., Zhao, W. Z., Xu, Z. M., Feng, Q., Xiao, S. C., & Xiao, H. L. (2014). Integrated study of the water-ecosystem-economy in the Heihe River Basin. *National Science Review*, *1*(3), 413–428. https://doi.org/10.1093/nsr/nwu017

Dai, Y., & Zeng, Q. (1997). A land surface model (IAP94) for climate studies Part I: Formulation and validation in off-line experiments. *Advances in Atmospheric Sciences*, *14*(4), 433–460.

Dai, Y. J., Zeng, X. B., Dickinson, R. E., Baker, I., Bonan, G. B., Bosilovich, M. G., et al. (2003). The common land model. *Bulletin of the American Meteorological Society*, *84*(8), 1013–1024. https://doi.org/10.1175/Bams-84-8-1013

Dickinson, R., Henderson-Sellers, A., & Kennedy, A. P. (2010). *Biosphere-atmosphere transfer scheme (BATS) version 1e as coupled to the NCAR community climate model*.

Dozier, J., & Frew, J. (1990). Rapid calculation OF terrain parameters for radiation modeling from digital elevation data. *IEEE Transactions on Geoscience and Remote Sensing*, *28*(5), 963–969. https://doi.org/10.1109/36.58986

Dubayah, R., & Loechel, S. (1997). Modeling topographic solar radiation using GOES data. *Journal of Applied Meteorology*, *36*(2), 141–154. https://doi.org/10.1175/1520-0450(1997)036<0141:mtsrug>2.0.co;2

Dubayah, R., & Rich, P. M. (1995). Topographic solar-radiation models for GIS. *International Journal of Geographical Information Systems*, *9*(4), 405–419. https://doi.org/10.1080/02693799508902046

Essery, R., & Marks, D. (2007). Scaling and parametrization of clear-sky solar radiation over complex topography. *Journal of Geophysical Research: Atmospheres*, *112*(D10). https://doi.org/10.1029/2006jd007650

Evans, K. F. (1998). The spherical harmonics discrete ordinate method for three-dimensional atmospheric radiative transfer. *Journal of the Atmospheric Sciences*, *55*(3), 429–446. https://doi.org/10.1175/1520-0469(1998)055<0429:Tshdom>2.0.Co;2

Fu, B. P. (1983). *Mountain climate* (in Chinese). Science Press.

Fu, P. D., & Rich, P. M. (2002). A geometric solar radiation model with applications in agriculture and forestry. *Computers and Electronics in Agriculture*, *37*(1–3), 25–35. https://doi.org/10.1016/s0168-1699(02)00115-1

Gu, C., Huang, A., Wu, Y., Yang, B., Mu, X., Zhang, X., & Cai, S. (2020). Effects of subgrid terrain radiative forcing on the ability of RegCM4.1 in the simulation of summer precipitation over China. *Journal of Geophysical Research: Atmospheres*, *125*(12), e2019JD032215. https://doi.org/10.1029/2019jd032215

Gu, L. H., Baldocchi, D., Verma, S. B., Black, T. A., Vesala, T., Falge, E. M., & Dowty, P. R. (2002). Advantages of diffuse radiation for terrestrial ecosystem productivity. *Journal of Geophysical Research*, *107*(D6), ACL 2-1-ACL 2-23. https://doi.org/10.1029/2001jd001242

Hao, D., Bisht, G., Gu, Y., Lee, W. L., Liou, K.-N., & Leung, L. R. (2021). A parameterization of sub-grid topographical effects on solar radiation in the E3SM land model: Implementation and evaluation over the Tibetan Plateau. *Geoscientific Model Development*, *14*(10), 6273–6289. https://doi.org/10.5194/gmd-2021-55

Hao, D., Wen, J., Xiao, Q., Wu, S. B., Lin, X., You, D., & Tang, Y. (2018). Modeling anisotropic reflectance over composite sloping terrain. *IEEE Transactions on Geoscience and Remote Sensing*, *56*(7), 3903–3923. https://doi.org/10.1109/Tgrs.2018.2816015

Hauge, G., & Hole, L. R. (2003). Implementation of slope irradiance in Mesoscale Model version 5 and its effect on temperature and wind fields during the breakup of a temperature inversion. *Journal of Geophysical Research: Atmospheres*, *108*(D2). https://doi.org/10.1029/2002jd002575

Hazenberg, P., Fang, Y., Broxton, P., Gochis, D., Niu, G. Y., Pelletier, J. D., et al. (2015). A hybrid-3D hillslope hydrological model for use in Earth system models. *Water Resources Research*, *51*(10), 8218–8239. https://doi.org/10.1002/2014wr016842

Helbig, N., & Löwe, H. (2012). Shortwave radiation parameterization scheme for subgrid topography. *Journal of Geophysical Research: Atmospheres*, *117*(D3). https://doi.org/10.1029/2011jd016465

Helbig, N., Löwe, H., & Lehning, M. (2009). Radiosity approach for the shortwave surface radiation balance in complex terrain. *Journal of the Atmospheric Sciences*, *66*(9), 2900–2912. https://doi.org/10.1175/2009jas2940.1

Huang, A., Zhao, Y., Zhou, Y., Yang, B., Zhang, L., Dong, X., et al. (2016). Evaluation of multisatellite precipitation products by use of ground-based data over China. *Journal of Geophysical Research: Atmospheres*, *121*(18), 10654–10675. https://doi.org/10.1002/2016jd025456

Huang, G., Liu, S., & Liang, S. (2012). Estimation of net surface shortwave radiation from MODIS data. *International Journal of Remote Sensing*, *33*(3), 804–825. https://doi.org/10.1080/01431161.2011.577834

Huang, P., Zhao, W., & Li, A. (2017). The preliminary investigation on the uncertainties associated with surface solar radiation estimation in mountainous areas. *IEEE Geoscience and Remote Sensing Letters*, *14*(7), 1071–1075. https://doi.org/10.1109/lgrs.2017.2696973

Hwang, T., Song, C. H., Vose, J. M., & Band, L. E. (2011). Topography-mediated controls on local vegetation phenology estimated from MODIS vegetation index. *Landscape Ecology*, *26*(4), 541–556. https://doi.org/10.1007/s10980-011-9580-8

Jarvis, A., Reuter, H. I., Nelson, A., & Guevara, E. (2008). *Hole-filled SRTM for the globe version 4*. International Centre for Tropical Agriculture (CIAT). Retrieved from http://srtm.csi.cgiar.org

Ji, P., Yuan, X., & Liang, X. Z. (2017). Do lateral flows matter for the hyperresolution land surface modeling? *Journal of Geophysical Research: Atmospheres*, *122*(22), 12077–12092. https://doi.org/10.1002/2017jd027366

Jimenez, P. A., & Dudhia, J. (2013). On the ability of the WRF model to reproduce the surface wind direction over complex terrain. *Journal of Applied Meteorology and Climatology*, *52*(7), 1610–1617. https://doi.org/10.1175/Jamc-D-12-0266.1

Jin, R., Kang, J., Xin, L. I., & Ma, M. (2015). *HiWATER: WATERNET observation dataset in the upper reaches of the Heihe River Basin (2014)*. National Tibetan Plateau Data Center. https://doi.org/10.3972/hiwater.221.2015.db

Jin, R., Li, X., Yan, B., Li, X., Luo, W., Ma, M., et al. (2014). A nested ecohydrological wireless sensor network for capturing the surface heterogeneity in the midstream areas of the Heihe River Basin, China. *IEEE Geoscience and Remote Sensing Letters*, *11*(11), 2015–2019. https://doi.org/10.1109/lgrs.2014.2319085

Kan, M., Huang, A., Zhao, Y., Zhou, Y., Yang, B., & Wu, H. (2015). Evaluation of the summer precipitation over China simulated by BCC_CSM model with different horizontal resolutions during the recent half century. *Journal of Geophysical Research: Atmospheres*, *120*(10), 4657–4670. https://doi.org/10.1002/2015jd023131

Kayiranga, A., Ndayisaba, F., Nahayo, L., Karamage, F., Nsengiyumva, J. B., Mupenzi, C., & Nyesheja, E. M. (2017). Analysis of climate and topography impacts on the spatial distribution of vegetation in the Virunga Volcanoes Massif of East-Central Africa. *Geosciences*, *7*(1), 17. https://doi.org/10.3390/geosciences7010017

Laio, F., D'Odorico, P., & Ridolfi, L. (2006). An analytical model to relate the vertical root distribution to climate and soil properties. *Geophysical Research Letters*, *33*(18). https://doi.org/10.1029/2006gl027331

Lee, W.-L., Liou, K.-N., Wang, C.-C., Gu, Y., Hsu, H.-H., & Li, J.-L. F. (2019). Impact of 3-D radiation-topography interactions on surface temperature and energy budget over the Tibetan Plateau in winter. *Journal of Geophysical Research: Atmospheres*, *124*(3), 1537–1549. https://doi.org/10.1029/2018jd029592

Li, J., & Li, X. (2007). Estimating solar radiation ON slope using DEM. *Acta Energiae Solaris Sinica*, *28*(8), 905–911.

Li, X., Cheng, G., Chen, X., & Lu, L. (1999). Modification of solar radiation model over rugged terrain. *Chinese Science Bulletin*, *44*(15), 1345–1349. https://doi.org/10.1007/bf02885977

Li, X., Cheng, G., Liu, S., Xiao, Q., Ma, M., Jin, R., et al. (2013). Heihe Watershed Allied Telemetry Experimental Research (HiWATER): Scientific objectives and experimental design. *Bulletin of the American Meteorological Society*, *94*(8), 1145–1160. https://doi.org/10.1175/bams-d-12-00154.1

Li, X., Koike, T., & Cheng, G. D. (2002). Retrieval of snow reflectance from Landsat data in rugged terrain. In J. G. Winther & R. Solberg (Eds.), *Annals of Glaciology* (Vol. 34, pp. 31–37). https://doi.org/10.3189/172756402781817635

Li, X., Li, X., Li, Z., Ma, M., Wang, J., Xiao, Q., et al. (2009). Watershed allied telemetry experimental research. *Journal of Geophysical Research: Atmospheres*, *114*(D22). https://doi.org/10.1029/2008jd011590

Liou, K. N., Gu, Y., Leung, L. R., Lee, W. L., & Fovell, R. G. (2013). A WRF simulation of the impact of 3-D radiative transfer on surface hydrology over the Rocky Mountains and Sierra Nevada. *Atmospheric Chemistry and Physics*, *13*(23), 11709–11721. https://doi.org/10.5194/acp-13-11709-2013

Liu, S., Li, X., Xu, Z., Che, T., Xiao, Q., Ma, M., et al. (2018). The Heihe Integrated Observatory Network: A basin-scale land surface processes observatory in China. *Vadose Zone Journal*, *17*(1), 180072. https://doi.org/10.2136/vzj2018.04.0072

Liu, S. M., Li, X., Che, T., Xu, Z. W., Zhang, Y., & Tan, J. L. (2016a). HiWATER: Dataset of hydrometeorological observation network (automatic weather station of A'rou shady slope station, 2014). *A Big Earth Data Platform for Three Poles*. https://doi.org/10.3972/hiwater.250.2015.db

Liu, S. M., Li, X., Che, T., Xu, Z. W., Zhang, Y., & Tan, J. L. (2016b). HiWATER: Dataset of hydrometeorological observation network (automatic weather station of A'rou sunny slope station, 2014). *A Big Earth Data Platform for Three Poles*. https://doi.org/10.3972/hiwater.249.2015.db

Luo, S., Lue, S., & Zhang, Y. (2009). Development and validation of the frozen soil parameterization scheme in Common Land Model. *Cold Regions Science and Technology*, *55*(1), 130–140. https://doi.org/10.1016/j.coldregions.2008.07.009

19422466, 2022, 1, Downloaded from https://agupubs.onlinelibrary.wiley.com/doi/10.1029/2021MS002654 by Anning Huang , Wiley Online Library on [22/03/2023]. See the Terms and Conditions (https://onlinelibrary.wiley.com/terms-and-conditions) on Wiley Online Library for rules of use; OA articles are governed by the applicable Creative Commons License

Ma, Y., & Liu, S. (2020). *High-temporal and Landsat-like surface evapotranspiration in Heihe River Basin (2010–2016) (HiTLL ET V1.0)*. National Tibetan Plateau Data Center. https://doi.org/10.11888/Hydro.tpdc.271081

Ma, Y., Liu, S., Song, L., Xu, Z., Liu, Y., Xu, T., & Zhu, Z. (2018). Estimation of daily evapotranspiration and irrigation water efficiency at a Landsat-like scale for an arid irrigation area using multi-source remote sensing data. *Remote Sensing of Environment*, *216*, 715–734. https://doi.org/10.1016/j.rse.2018.07.019

Mao, K. B. (2020). A combined Terra and Aqua MODIS land surface temperature and meteorological station data product for China (2003-2017). *A Big Earth Data Platform for Three Poles*. https://doi.org/10.5281/zenodo.3528024

Marsh, C. B., Pomeroy, J. W., & Spiteri, R. J. (2012). Implications of mountain shading on calculating energy for snowmelt using unstructured triangular meshes. *Hydrological Processes*, *26*(12), 1767–1778. https://doi.org/10.1002/hyp.9329

Muller, M. D., & Scherer, D. (2005). A grid- and subgrid-scale radiation parameterization of topographic effects for mesoscale weather forecast models. *Monthly Weather Review*, *133*(6), 1431–1442. https://doi.org/10.1175/mwr2927.1

Nian, G. (2020). *Numerical simulation of the effect of the terrain radiation on Tibetan Plateau and Asian monsoon*. Institute of Atmospheric Physics, Chinese Academy of Sciences.

Pan, X., Li, X., Cheng, G., Li, H., & He, X. (2015). Development and evaluation of a river-basin-scale high spatio-temporal precipitation data set using the WRF model: A case study of the Heihe River Basin. *Remote Sensing*, *7*(7), 9230–9252. https://doi.org/10.3390/rs70709230

Pan, X., Li, X., Shi, X., Han, X., Luo, L., & Wang, L. (2012). Dynamic downscaling of near-surface air temperature at the basin scale using WRF-a case study in the Heihe River Basin, China. *Frontiers of Earth Science*, *6*(3), 314–323. https://doi.org/10.1007/s11707-012-0306-2

Pan, X., & Ma, H. (2019). Near-surface hourly atmospheric driving data at 0.05°×0.05° based on WRF model simulation over 2000–2016 years for the Heihe River Basin. *Plateau Meteorology*, *38*(1), 206–216.

Pan, X. D. (2020). *The atmospheric forcing data in the Heihe River Basin (2000–2018)*. National Tibetan Plateau Data Center. https://doi.org/10.11888/Meteoro.tpdc.271245

Reda, I., & Andreas, A. (2007). Corrigendum to "Solar position algorithm for solar radiation applications" [Solar Energy 76 (2004) 577–589]. *Solar Energy*, *81*(6), 838. https://doi.org/10.1016/j.solener.2007.01.003

Rieu, M., & Sposito, G. (1991). Fractal fragmentation, soil porosity, and soil-water properties. 1. Theory. *Soil Science Society of America Journal*, *55*(5), 1231–1238. https://doi.org/10.2136/sssaj1991.03615995005500050006x

Ruiz-Arias, J. A., Cebecauer, T., Tovar-Pescador, J., & Suri, M. (2010). Spatial disaggregation of satellite-derived irradiance using a high-resolution digital elevation model. *Solar Energy*, *84*(9), 1644–1657. https://doi.org/10.1016/j.solener.2010.06.002

Ruiz-Arias, J. A., Pozo-Vazquez, D., Lara-Fanego, V., Santos-Alamillos, F. J., & Tovar-Pescador, J. (2011). A high-resolution topographic correction method for clear-sky solar irradiance derived with a numerical weather prediction model. *Journal of Applied Meteorology and Climatology*, *50*(12), 2460–2472. https://doi.org/10.1175/2011jamc2571.1

Ruiz-Arias, J. A., Tovar-Pescador, J., Pozo-Vazquez, D., & Alsamamra, H. (2009). A comparative analysis of DEM-based models to estimate the solar radiation in mountainous terrain. *International Journal of Geographical Information Science*, *23*(8), 1049–1076. https://doi.org/10.1080/13658810802022806

Shen, C. P., & Phanikumar, M. S. (2010). A process-based, distributed hydrologic model based on a large-scale method for surface-subsurface coupling. *Advances in Water Resources*, *33*(12), 1524–1541. https://doi.org/10.1016/j.advwatres.2010.09.002

Shen, Y., & Hu, J. (2006). Slope irradiance scheme in GRAPES and its effect on simulation of short-range weather processes. *Chinese Journal of Atmospheric Sciences*, *30*(6), 1129–1137.

Song, Y., Guo, W., & Zhang, Y. (2008). Simulation of latent heat flux exchange between land surface and atmosphere in temperate mixed forest and subtropical artificial coniferous forest sites in China by CoLM. *Plateau Meteorology*, *27*(5), 967–977.

Tang, B., Li, Z.-L., & Zhang, R. (2006). A direct method for estimating net surface shortwave radiation from MODIS data. *Remote Sensing of Environment*, *103*(1), 115–126. https://doi.org/10.1016/j.rse.2006.04.008

Tang, W., Yang, K., He, J., & Qin, J. (2010). Quality control and estimation of global solar radiation in China. *Solar Energy*, *84*(3), 466–475. https://doi.org/10.1016/j.solener.2010.01.006

Taylor, K. E. (2001). Summarizing multiple aspects of model performance in a single diagram. *Journal of Geophysical Research: Atmospheres*, *106*(D7), 7183–7192. https://doi.org/10.1029/2000jd900719

Vignola, F., Harlan, P., Perez, R., & Kiniecik, M. (2007). Analysis of satellite derived beam and global solar radiation data. *Solar Energy*, *81*(6), 768–772. https://doi.org/10.1016/j.solener.2006.10.003

Wang, T., Yan, G., & Chen, L. (2012). Consistent retrieval methods to estimate land surface shortwave and longwave radiative flux components under clear-sky conditions. *Remote Sensing of Environment*, *124*, 61–71. https://doi.org/10.1016/j.rse.2012.04.026

Wang, T., Yan, G., Mu, X., Jiao, Z., Chen, L., & Chu, Q. (2018). Toward operational shortwave radiation modeling and retrieval over rugged terrain. *Remote Sensing of Environment*, *205*, 419–433. https://doi.org/10.1016/j.rse.2017.11.006

Wang, X. J., Pang, G. J., & Yang, M. X. (2018). Precipitation over the Tibetan Plateau during recent decades: A review based on observations and simulations. *International Journal of Climatology*, *38*(3), 1116–1131. https://doi.org/10.1002/joc.5246

Wood, S. W., Murphy, B. P., & Bowman, D. M. J. S. (2011). Firescape ecology: How topography determines the contrasting distribution of fire and rain forest in the south-west of the Tasmanian Wilderness World Heritage Area. *Journal of Biogeography*, *38*(9), 1807–1820. https://doi.org/10.1111/j.1365-2699.2011.02524.x

Wu, C. M., Lo, M. H., Chen, W. T., & Lu, C. T. (2015). The impacts of heterogeneous land surface fluxes on the diurnal cycle precipitation: A framework for improving the GCM representation of land-atmosphere interactions. *Journal of Geophysical Research: Atmospheres*, *120*(9), 3714–3727. https://doi.org/10.1002/2014jd023030

Wu, S., Wen, J., You, D., Zhang, H., Xiao, Q., & Liu, Q. (2018). Algorithms for calculating topographic parameters and their uncertainties in downward surface solar radiation (DSSR) estimation. *IEEE Geoscience and Remote Sensing Letters*, *15*(8), 1149–1153. https://doi.org/10.1109/lgrs.2018.2831916

Xin, Y., Bian, L., & Zhang, X. (2006). The application of CoLM to arid region of northwest China and Qinghai-Xizang Plateau. *Plateau Meteorology*, *25*(4), 567–574.

Zhang, X., Liang, S., Song, Z., Niu, H., Wang, G., Tang, W., et al. (2016). Local adaptive calibration of the satellite-derived surface incident shortwave radiation product using smoothing spline. *IEEE Transactions on Geoscience and Remote Sensing*, *54*(2), 1156–1169. https://doi.org/10.1109/tgrs.2015.2475615

Zhang, X., Liang, S., Zhou, G., Wu, H., & Zhao, X. (2014). Generating Global LAnd Surface Satellite incident shortwave radiation and photosynthetically active radiation products from multiple satellite data. *Remote Sensing of Environment*, *152*, 318–332. https://doi.org/10.1016/j.rse.2014.07.003

Zhang, Y., Huang, A., & Zhu, X. (2006). Parameterization of the thermal impacts of sub-grid orography on numerical modeling of the surface energy budget over East Asia. *Theoretical and Applied Climatology*, *86*(1–4), 201–214. https://doi.org/10.1007/s00704-005-0209-1

19422466, 2022, 1, Downloaded from https://agupubs.onlinelibrary.wiley.com/doi/10.1029/2021MS002654 by Anning Huang , Wiley Online Library on [22/03/2023]. See the Terms and Conditions (https://onlinelibrary.wiley.com/terms-and-conditions) on Wiley Online Library for rules of use; OA articles are governed by the applicable Creative Commons License

Zhang, Y. L., Li, X., Cheng, G. D., Jin, H. J., Yang, D. W., Flerchinger, G. N., et al. (2018). Influences of topographic shadows on the thermal and hydrological processes in a cold region mountainous watershed in northwest China. *Journal of Advances in Modeling Earth Systems*, *10*(7), 1439–1457. https://doi.org/10.1029/2017ms001264

Zhao, B., Mao, K., Cai, Y., Shi, J., Li, Z., Qin, Z., et al. (2020). A combined Terra and Aqua MODIS land surface temperature and meteorological station data product for China from 2003 to 2017. *Earth System Science Data*, *12*(4), 2555–2577. https://doi.org/10.5194/essd-12-2555-2020

Zhu, K. F., Xue, M., Zhou, B. W., Zhao, K., Sun, Z. Q., Fu, P. L., et al. (2018). Evaluation of real-time convection-permitting precipitation forecasts in China during the 2013–2014 summer season. *Journal of Geophysical Research: Atmospheres*, *123*(2), 1037–1064. https://doi.org/10.1002/2017jd027445

19422466, 2022, 1, Downloaded from https://agupubs.onlinelibrary.wiley.com/doi/10.1029/2021MS002654 by Anning Huang , Wiley Online Library on [22/03/2023]. See the Terms and Conditions (https://onlinelibrary.wiley.com/terms-and-conditions) on Wiley Online Library for rules of use; OA articles are governed by the applicable Creative Commons License